



**Computer Simulation of the Destruction of a
Close-In Diagnostic for the Laboratory
Microfusion Facility**

R.R. Peterson

August 1989

UWFDM-798

FUSION TECHNOLOGY INSTITUTE

UNIVERSITY OF WISCONSIN

MADISON WISCONSIN

DISCLAIMER

This report was prepared as an account of work sponsored by an agency of the United States Government. Neither the United States Government, nor any agency thereof, nor any of their employees, makes any warranty, express or implied, or assumes any legal liability or responsibility for the accuracy, completeness, or usefulness of any information, apparatus, product, or process disclosed, or represents that its use would not infringe privately owned rights. Reference herein to any specific commercial product, process, or service by trade name, trademark, manufacturer, or otherwise, does not necessarily constitute or imply its endorsement, recommendation, or favoring by the United States Government or any agency thereof. The views and opinions of authors expressed herein do not necessarily state or reflect those of the United States Government or any agency thereof.

**Computer Simulation of the Destruction of a
Close-In Diagnostic for the Laboratory
Microfusion Facility**

R.R. Peterson

Fusion Technology Institute
University of Wisconsin
1500 Engineering Drive
Madison, WI 53706

<http://fti.neep.wisc.edu>

August 1989

UWFDM-798

I. INTRODUCTION

The Laboratory Microfusion Facility (LMF) [1] would be the first facility to routinely explode high yield Inertial Confinement Fusion (ICF) pellets. There are several reasons in building the LMF, one being the development of high gain targets for use in ICF reactors. To develop targets, one must diagnose the performance of experimental targets in the act of burning [2]. One might require that the target diagnostics be placed only a few cm from the target. One concept for such a "close-in" diagnostic, developed at Lawrence Livermore National Laboratory (LLNL) [3], is shown in Fig. 1. This concept has a lead shield encased in an aluminum capsule. The actual diagnostic would be placed inside the cavity at the back of the lead.

Once high yield is achieved, the target diagnostic will be destroyed. Intense x-rays emanating from the target will deposit in the aluminum on the front of the diagnostic package. These x-rays create a very high energy density in the aluminum that leads to extremely high pressures that launch strong shock waves into the material. These shock waves destroy the diagnostic package and accelerate pieces of it to high velocity. The shrapnel generated in this process represents a threat to the target chamber wall or objects that are inside the LMF target chamber.

In this paper, I will present results of two-dimensional simulations of the x-ray driven destruction of the diagnostic package shown in Fig. 1. I will describe the methods used in the simulation and the models used to study the fragmentation of the diagnostics package into shrapnel. I will then list the assumptions I have used as to the target chamber parameters and will use some simple models to estimate the effect that the x-rays will have on the diagnostics package. I will then present results that graphically show a shock front moving

through the diagnostic. Finally, I will discuss the fragmentation of the material into shapnel.

II. METHODS OF ANALYSIS AND SIMULATION

I have used the CSQ computer code to simulate the break-up of the close-in diagnostic shown in Fig. 1. CSQ is a two-dimensional Eulerian hydrodynamics code that was written and is maintained at Sandia National Laboratory (SNL) [4]. CSQ can model many of the phenomena important to shock waves propagating in solids including phase transitions in solids, elastic/plastic flow, and the crushing of porous materials. However, CSQ does not do a good enough job of radiation transport for this problem, so I have coupled it to a code that does a better job of radiation transport [5]. In this way we can adequately transport and deposit the target x-rays and, at the same time, correctly model the propagation of the shock.

The results of the CSQ simulation provide a detailed two-dimensional picture of the hydrodynamic motion in the diagnostic package. With this information, one can estimate the rate at which the density of a section of the diagnostics package is changing. This is equivalent to the strain rate. One can then use the Grady model [6] to estimate the size of the fragments into which the diagnostic package will break, and the momentum and energy that the fragments will contain.

The Grady model uses an energy method to calculate the average size of fragments created by hydromotion in matter. For something to break into fragments, there must be enough free energy in the system to provide the surface energy of the fragments. In a liquid, the surface energy is the surface energy per unit area times the surface area; in a solid, it is the fracture toughness times the surface area. The greater the free energy available, the more surface

area of fragments, and thus the smaller are fragments created because smaller particles have a larger surface to volume ratio. Also, fragment size will increase as the surface energy per unit area or the fracture toughness increases. In the Grady model, the free energy comes from the kinetic energy about the center-of-mass of each piece of material that is to become a fragment. Conservation of momentum requires that the kinetic energy of the center-of-mass of a piece of material does not change, so this energy is not available for conversion into surface energy. These principles lead to the following expressions for average fragment size for liquids,

$$d = 7.11 (\rho \gamma / \dot{\rho}^2)^{1/3}, \quad (1)$$

where d is the fragment diameter, ρ is the mass density, $\dot{\rho}$ is the time rate of change of ρ and γ is the surface energy per unit area; or,

$$d = 2.72 (K_{IC} / \rho \dot{\epsilon} C_s)^{2/3}, \quad (2)$$

for solids, where K_{IC} is the fracture toughness,

Error!

III. LMF PARAMETERS AND SIMPLE PREDICTIONS

I have had to make some assumptions regarding the performance of the ICF target on the diagnostic package. The parameters for the LMF and some predictions based on these parameters are shown in Table 1. I have assumed that the target releases 1000 MJ of total energy when it burns, and that 220 MJ are in x-rays. This is consistent with the "HIBALL" target [7]. This target releases x-rays with the spectrum shown in Fig. 2 and I have assumed that it

Table 1. LMF Target Diagnostics Parameters

Total Target Yield	1000 MJ
Target Type	"HIBALL" Ion Beam Target
Energy in X-rays	220 MJ
Peak Photon Energy	1 keV
X-Ray Pulse Width	1 ns
Target Chamber Gas	1 torr Argon
Distance from Target to Front of Diagnostics Package	5 cm
X-ray Fluence	700 kJ/cm ²
E-folding Length of 1 keV X-rays in Al	3.7 microns
Energy Density in Al	1893 MJ/cm ³
Pressure (Grueneisen)	40 Gbar
Specific Energy in Al	700 MJ/g
Temperature in Al (SESAME)	10 keV
Pressure in Al (SESAME)	20 Gbar
X-ray Power Intensity	700 TW/cm ²
Speed of Sound	37 km/s
Pressure in Al (0.35 Ix / C _s)	660 Mbar

releases this energy in a Gaussian pulse in time, with a 1 ns FWHM. The target chamber is filled with 1 torr of argon, though the distance between the target and the diagnostics package is short enough that the presence of the gas probably makes little difference to the response of the diagnostic package to the x-rays. I have neglected the effects of target debris because the shock generated in the solid material will have had time to move into the material before the debris ions reach the surface. I have assumed that the aluminum front surface of the diagnostic is slightly curved so that all parts of the surface are the same distance from the target, that is, 5 cm from the target. The distance into the aluminum at which the x-ray intensity falls by $1/e$ for 1 keV x-rays is 3.7 microns [8].

From these parameters, one can estimate the energy density, the power density and, therefore, the pressure in the aluminum. I have estimated the pressure in three ways. From these numbers, one can estimate an energy density of 1893 MJ/cm^3 and a specific energy of 700 MJ/g (the mass density of aluminum is 2.7 g/cm^3). I arrived at these numbers by assuming that all of the energy is uniformly deposited within the e-folding length, and is therefore an overestimate of the average value within the e-folding length by less than a factor of two, but is much closer to the value on the surface. The simplest way to estimate the pressure is as the product of the energy density and the Grueneisen coefficient, which is 2.1 for aluminum near room temperature. This gives an estimate for the pressure of 40 Gbar. From the SESAME equation-of-state tables [9], which take into account the high temperature behavior, the material should reach a temperature of 1 keV and a pressure of 20 Gbar. These estimates neglect the movement of the energy through the material while energy is being deposited, the effect being a reduction in the energy density and pressure. Elsewhere [10], I have discussed how one can, taking this effect into account, estimate the x-ray driven pressure to be approximately 0.35 times the x-

ray intensity divided by the speed of sound. This is based on the assumption that the energy spreads through the material at the speed of sound, and where the normalization factor of 0.35 is based on comparisons with experiment and computer simulations. The pressure estimated in this manner is 660 Mbar. Therefore, in three ways, I have shown that one should expect pressures of at least a few hundred Mbars on the surface of the diagnostic package nearest the target. This pressure is clearly large enough to generate strong shock waves. In the next section, I will present a more quantitative picture with the help of computer simulations.

IV. RESULTS OF COMPUTER SIMULATIONS

From the estimates in the previous section, it is clear that the material nearest the target in the diagnostics package will experience pressures at least on the order of hundreds of Mbars. With the use of computer simulation, one can consider the generation and propagation of shocks into the two-dimensional structure of the diagnostics package. This approach will also allow the calculation of the velocity of material that is ejected from the diagnostics package in the form of shrapnel. As discussed in Section II, I have used the CSQ code for these simulations. The results of these simulations are shown graphically in Fig. 3 through Fig. 39. CSQ has a scheme allowing it to only calculate in regions of the mesh where something is actually happening. Therefore, in these plots, only those parts of the mesh that are active are visible.

The first group of these pictures, Fig. 3 through Fig. 14, are plots of the pressure at various times over the two-dimensional spatial mesh of the simulation. The times are measured from the end of x-ray deposition. The view is from the back of the diagnostic. The diagnostics package and the simulation both have cylindrical symmetry about a center line. The y-axis is along the axis

of symmetry of the package and has its origin at the original front surface along the axis of symmetry. The x-axis is in the direction transverse to the axis of symmetry and has its origin at the package's centerline. The plots represent what one would see on a plane exposed by a transverse cut down the axis of symmetry. One can see in Fig. 3 that the pressure 1 ns after the end of deposition is about 95 Mbar, lower than all of the estimates in the previous section but still a large value. The time since the onset of x-ray deposition is 2 ns, twice the pulse width, so the maximum pressure may be close to 200 Mbar. At 10 ns, the pressure seen in Fig. 4 has fallen to about 35 Mbar and is still fairly uniform across the shock front. At 50 ns, Fig. 5, one sees the shock start to run down the outside edge of the package. This process continues at 100 ns, and as seen in Fig. 6, the pressure across the shock that is moving through the main body of the material is still fairly uniform. At 250 ns, Fig. 7, one begins to notice a lower pressure in the center of the shock front and a higher value near the edges, and one still sees the shock racing ahead outside the diagnostics package. These trends continue at 450 ns, 750 ns, and 1 microsecond, which are shown in Figs. 8, 9, and 10. By 1 microsecond, the peak pressure has fallen to slightly more than 2 Mbar. At 2 microseconds one can see in Fig. 11 the shock beginning to break out in the central slot at the back of the diagnostic. One can also begin to guess why the shock is stronger away from the middle: the absence of mass in the center leads to a relieving of the shock pressure. In Fig. 12 one sees that by 3 microseconds the complicated shape of the package leads to a breaking up of the planar shock front into several weaker shocks. This continues at 4 and 5 microseconds, Figs. 13 and 14, where one sees blown off material moving out beyond the original back surface of the lead and that pressures are still as high as 100 kbar.

In Figs. 15 through 26, I show the densities at the same times that I previously showed the pressures. Initially, one can see material being blown off of the front surface and around the outside edges of the diagnostic package. One can see a high density peak growing as the planar shock develops in the early stages of the problem. At 1 microsecond, Fig. 22, one can see a central reduction in the density corresponding to that feature in the pressure profiles. One can also see the material ahead of the shock in the center has begun to move, perhaps indicating the pressure relief suggested in the preceding paragraph. In Figs. 23 through 26 (2, 3, 4, and 5 microseconds), one sees material being blown off from the back of the lead in the slot and the complicated structure that results.

Another way of displaying these effects is by showing velocities and material interfaces developing in a two-dimensional plane. These plots are shown in Figs. 27 through 38 at the same times as the pressures and densities. The velocities are depicted on the left-hand side of the figures by arrows, where there is one arrow for each active Eulerian mesh. The length of the stem of each arrow indicates the speed and a scale is shown on the right. The material outside of the diagnostic package is argon, and as one moves toward the centerline, the materials change to aluminum and then lead. In the central slot, there is a void. In Fig. 27, one sees the package 1 ns after the end of the x-ray, where material is blowing off of the surface of the aluminum casing at about 40 km/s. The aluminum also moves laterally out beyond the edge of the original casing. One can also see blowoff motion in the lead region. At 10 ns, Fig. 28, the blowoff continues and the aluminum begins to be pushed back along the outside edge of the package at about 60 km/s. At 50 ns the front part of the aluminum has been completely vaporized and one can see the vapor cloud moving back along the outside at 100 km/s. At 100 ns, Fig. 30, the same

features are present. At 250 ns the lead begins to move and one can see it begin to spread laterally. This continues at 450 ns and one can now clearly see shock motion into the lead. The same continues at 750 ns and 1 microsecond. At 2 microseconds, Fig. 35, the shock reaches the edge of the central slot and lead vapor has spread over a large area. In Fig. 36, 3 microseconds, one sees a mass of lead moving down the central slot at 5 km/s. One would expect this blown off material to have a velocity of twice the particle velocity behind the shock just before the shock reaches the back of the lead [11]. From Fig. 11, the pressure of the shock just prior to reaching the slot is roughly 1 Mbar, and from Fig. 23 the density is 15 g/cm³. From the LASL shock Hugoniot data [12] a shock in lead with a pressure of 1 Mbar should have a particle velocity of 1.8 km/s, which would lead us to expect a blowoff velocity of 3.6 km/s, somewhat less than what the code predicts. The value of 5 km/s is the speed at which the lead/void interface is moving 1 microsecond after the initial release of material from the back of the lead. If the lead is vapor, there is a large pressure gradient that will further accelerate the lead that could lead to the discrepancy. The velocity profile along the centerline of the diagnostics package at 5 microseconds is shown in Fig. 39. One sees that the material is not a solid but is an expanding gas. One can see that beyond the end of the solid lead, which is at 4.5 cm, the gas expands radially. At 2, 3, 4, and 5 microseconds one sees the lead pushing out the aluminum casing. By comparing the positions of the lead/aluminum interfaces in Figs. 35, 36, 37, and 38, one finds that the aluminum is being pushed at a velocity of about 5 km/s. In Fig. 38, one sees that the slug of material blown off of the central slot has begun to spread out into the void behind the bulk of the lead.

V. FRAGMENTATION

I have calculated the sizes of fragments into which the aluminum casing is broken by the shock motion of the lead. From the CSQ simulations, I have determined that the casing is being pushed outward at 5 km/s. In an expanding cylinder, the time rate-of-change of the mass density is

$$\dot{\rho} = \rho V / R \quad (3)$$

where V is the velocity. The strain rate for a cylinder is

$$\begin{aligned} \dot{\epsilon} &= \dot{\rho} / 3 \rho \quad (4) \\ &= V / 3 R . \end{aligned} \quad (5)$$

Therefore, the size of the fragments is

$$d = 2.72 (3 K_R / \rho V C_s)^{2/3} . \quad (6)$$

For aluminum, ρ is 2.7 g/cm³, C_s is 6.4 km/s and K_{IC} is 25 Mn m^{-3/2}. V is 5 km/s and R is about 1 cm. Substitution of these parameters into eqn. 6 leads to a fragment diameter of 5.5×10^{-2} cm. The mass of such a fragment is 1.9 milligrams, its velocity is 5 km/s, its momentum is 950 g-cm/s, and its kinetic energy is 24 J.

The material that comes off of the back of the lead is not in solid fragments and the material that is vaporized from the front surface is individual atoms. This material can have even higher velocities than the fragments, though the energy and momentum of each particle would be much less.

With this analysis, I have not been able as yet to determine the ultimate condition of the aluminum casing beyond the lead region. The lead that is blown off of the back of the diagnostics package will eventually fill the void inside the aluminum tube with some pressure which may cause additional fragmentation, or it may just deform the tube. Whatever the case, the region containing the lead

will be destroyed and the package will obviously need to be replaced after every shot. The only question is whether or not some parts of the aluminum tube will remain. If the lower parts of the tube are fragmented, the fragment velocities will be much less than for those coming from the aluminum casing around the lead.

VI. CONCLUSIONS

I have used the CSQ computer code to simulate the breakup of a close-in target diagnostics package for the LMF. I have used an analytic method to consider the fragmentation of part of this package. The remaining task is to consider the presence of this shrapnel when considering LMF target chamber design.

ACKNOWLEDGMENTS

The work has been supported by Lawrence Livermore National Laboratory and by Sandia National Laboratories. This work was performed while the author was on an extended visit to Sandia National Laboratories and computer calculations were performed on Sandia's computers.

REFERENCES

1. LMF - Laboratory Microfusion Capability Study, Phase-I Summary, DOE/DP-0069.
2. See, for example, R.L. McCrory, et al., "High-Density Laser-Fusion Experiments at the Laboratory for Laser Energetics," Laser Interaction and Related Plasma Phenomena, vol. 8 (Plenum Press, New York, 1988), H. Hora and G.H. Miley, editors, p. 498.
3. Monya Lane, Lawrence Livermore National Laboratory, private communication.
4. S.L. Thompson and J.M. McGlaun, "CSQIII, An Eulerian Finite Difference Program for Two-Dimensional Material Response: Users Manual," Sandia National Laboratories Report SAND87-2763 (January, 1988).
5. A.V. Farnsworth, "LASTRAN: A System for Coupling the LASNEX and CSQ Hydrocodes," Sandia National Laboratories Report SAND86-0866 (July, 1986).
6. D.E. Grady, "Local Inertial Effects in Dynamic Fragmentation," J. Appl. Phys. 53, 322 (1982).
7. G.A. Moses, R.R. Peterson, M.E. Sawan, and W.F. Vogelsang, "High Gain Target Spectra and Energy Partitioning for Ion Beam Reactor Design Studies," University of Wisconsin Fusion Technology Institute Report UWFD-396 (1980).
8. F. Biggs and R. Lighthill, "Analytic Approximations for X-Ray Cross Sections III," Sandia National Laboratories Report SAND87-0070 (August, 1988).
9. "T-4 Handbook of Material Properties Data Bases, vol. 1c: Equations of State," K.S. Holian, editor, Los Alamos National Laboratories Report LA-10160-MS (November, 1984).
10. J.J. MacFarlane, et al., "Inertial Confinement Fusion Reactor Cavity Analysis: Report for the Period 1 July 1988 to 30 June 1989," University of Wisconsin Fusion Technology Institute Report UWFD-793 (July, 1989).
11. Ya.B. Zel'dovich and Yu.P. Raiser, "Physics of Shock Waves and High Temperature Hydrodynamic Phenomena," (Academic Press, New York, 1967).
12. "LASL Shock Hugoniot Data," Stanley P. Marsh, editor (University of California Press, Berkeley, California, 1980).

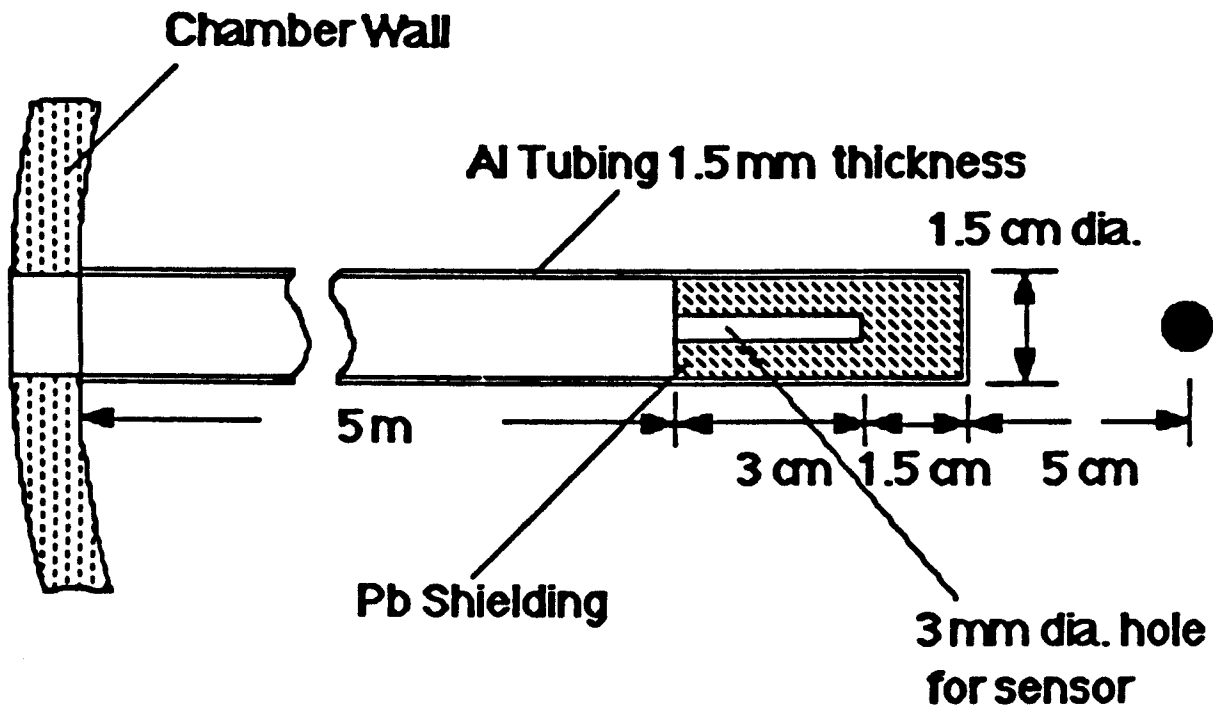


Fig. 1. Schematic picture of a close-in target diagnostic package.

Yield = 1000 MJ

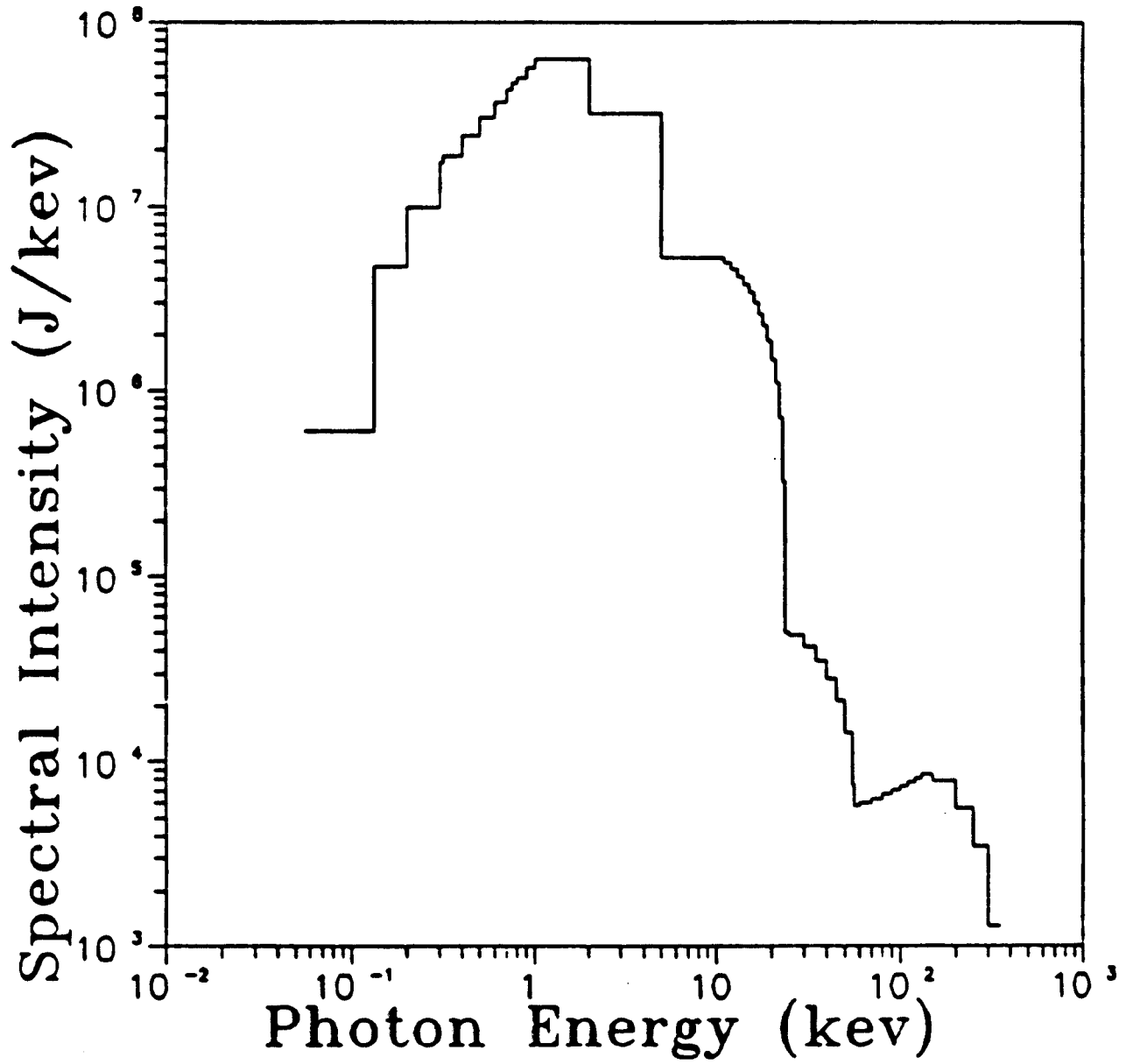


Fig. 2. X-Ray spectrum from HIBALL target.

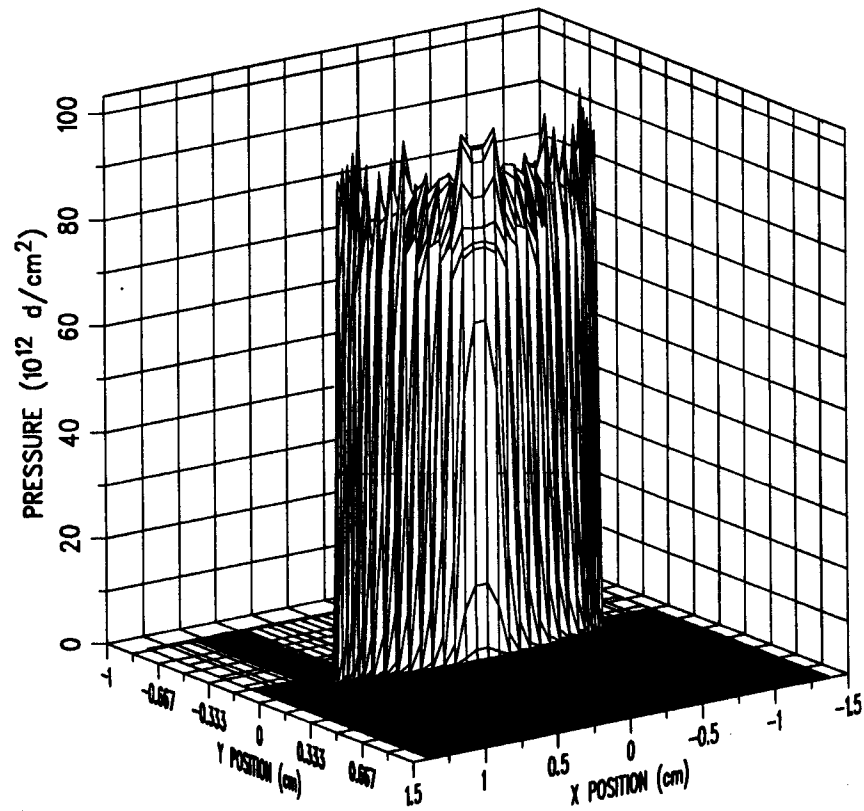


Fig. 3. Pressure profile 1.0 nanoseconds after end of x-ray deposition.

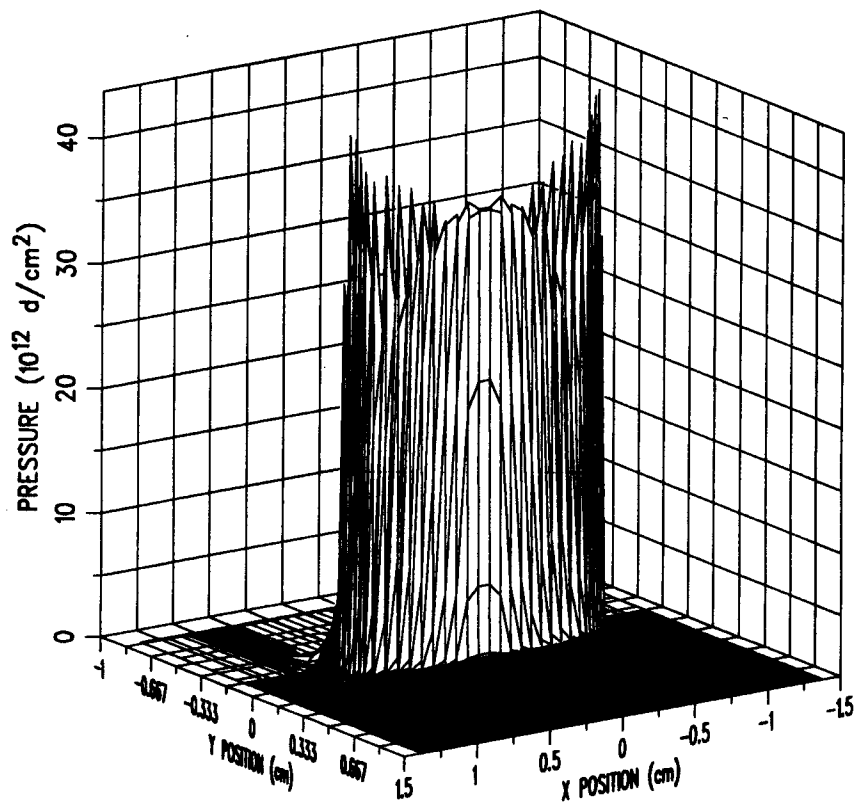


Fig. 4. Pressure profile 10.0 nanoseconds after end of x-ray deposition.

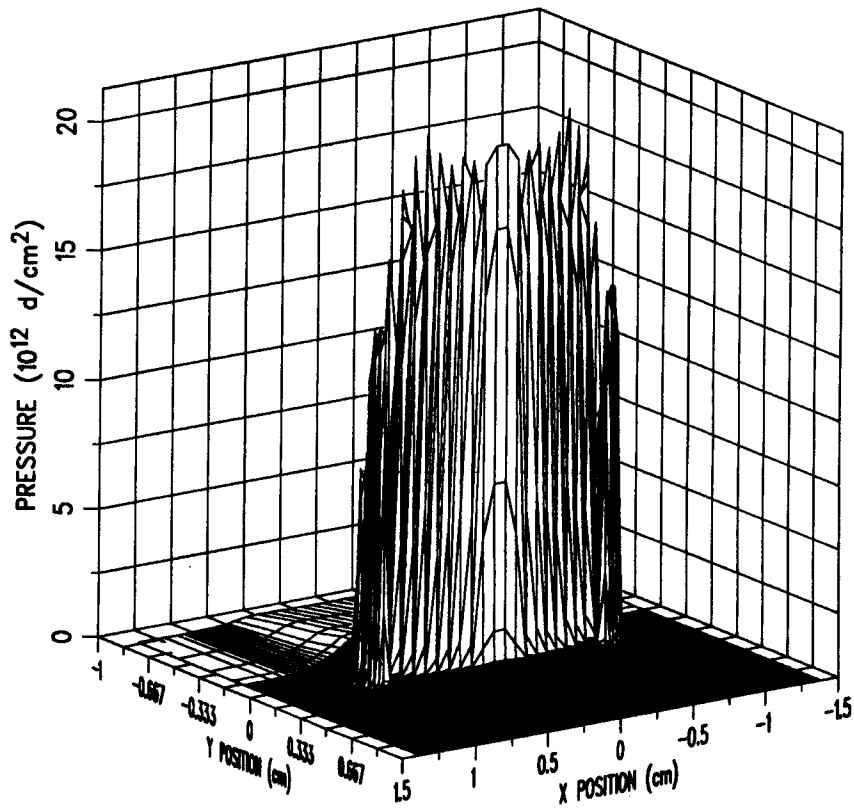


Fig. 5. Pressure profile 50.0 nanoseconds after end of x-ray deposition.

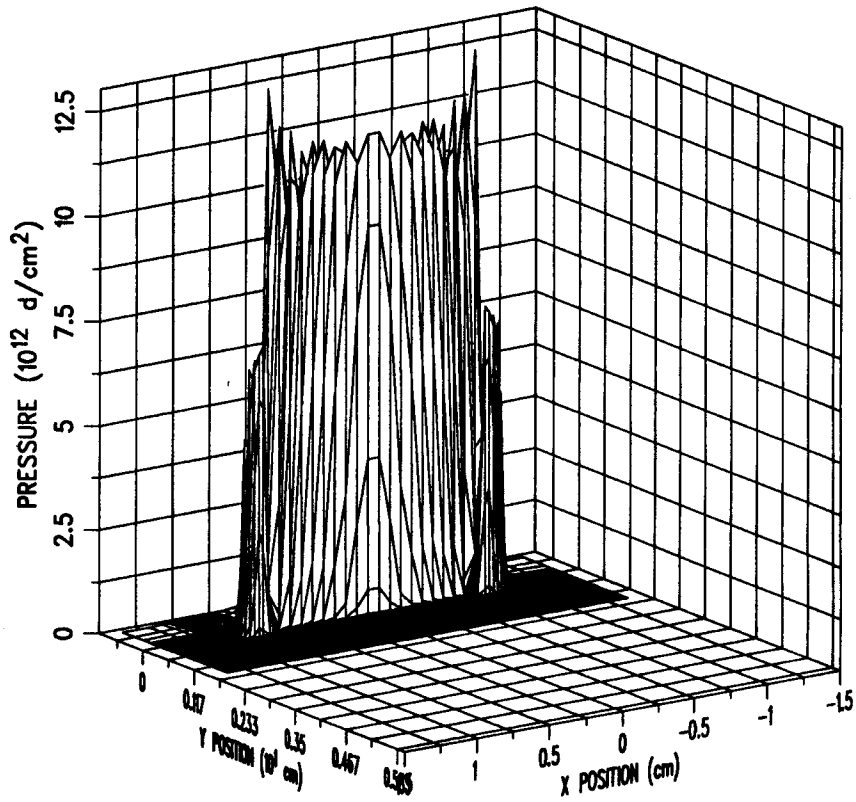


Fig. 6. Pressure profile 100.0 nanoseconds after end of x-ray deposition.

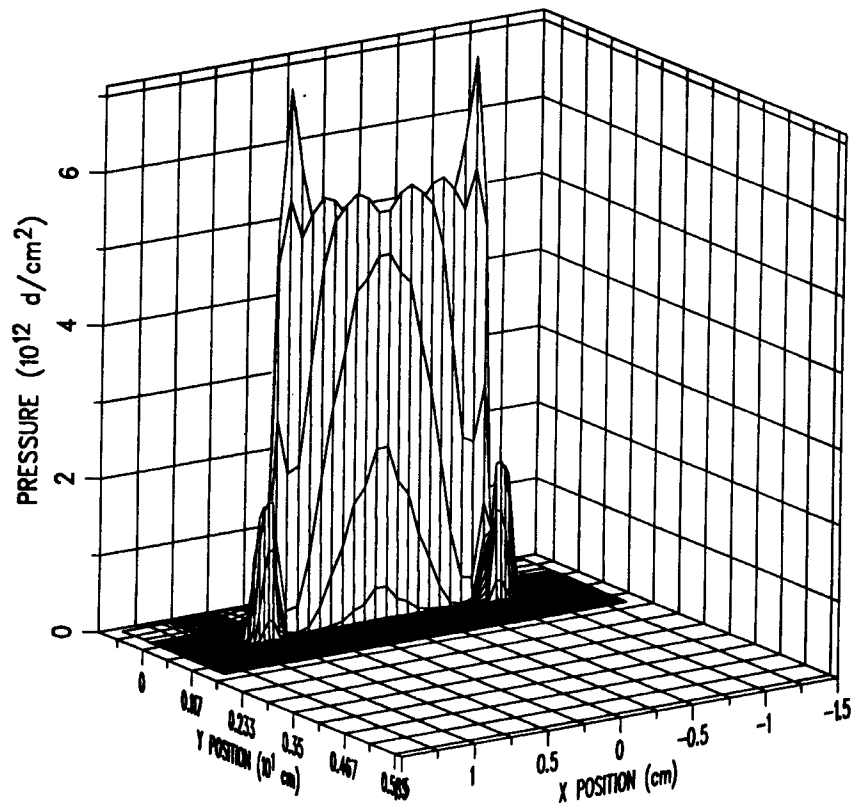


Fig. 7. Pressure profile 250.0 nanoseconds after end of x-ray deposition.

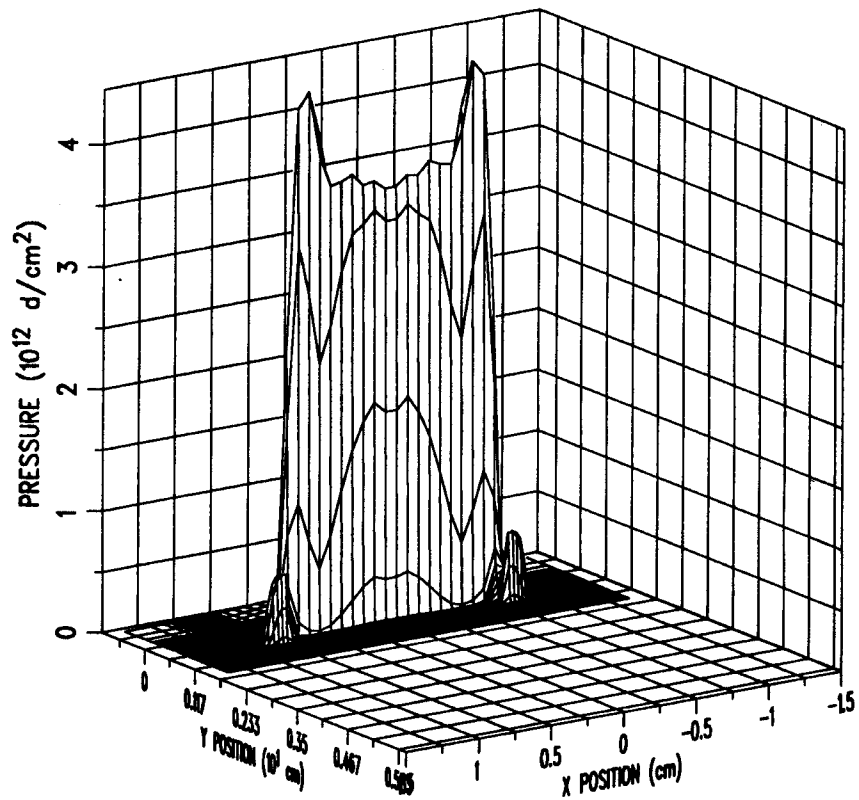


Fig. 8. Pressure profile 450.0 nanoseconds after end of x-ray deposition.

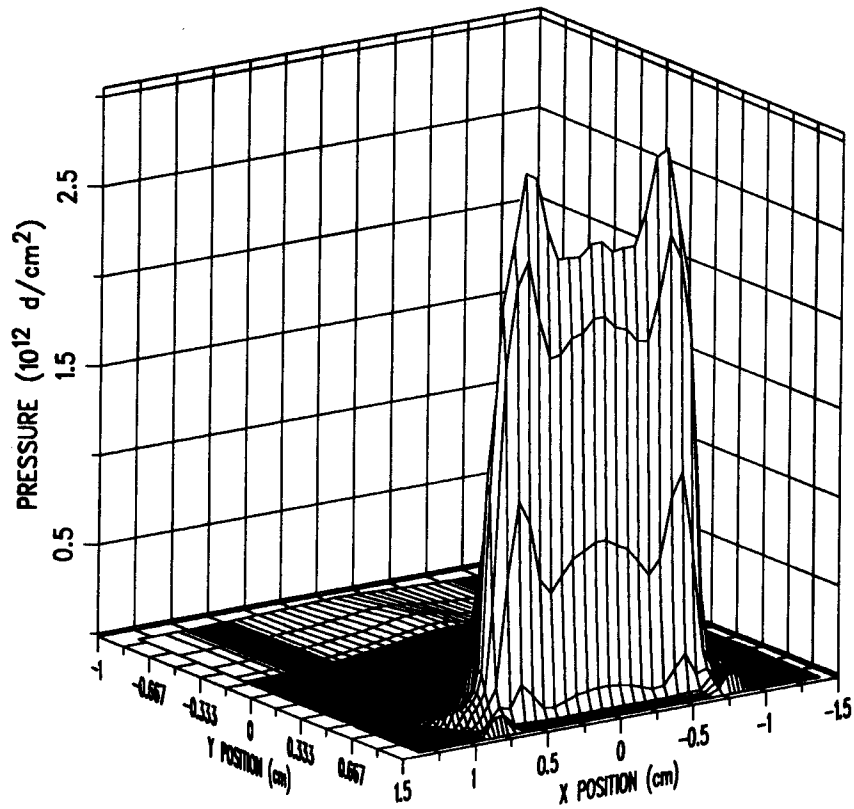


Fig. 9. Pressure profile 750.0 nanoseconds after end of x-ray deposition.

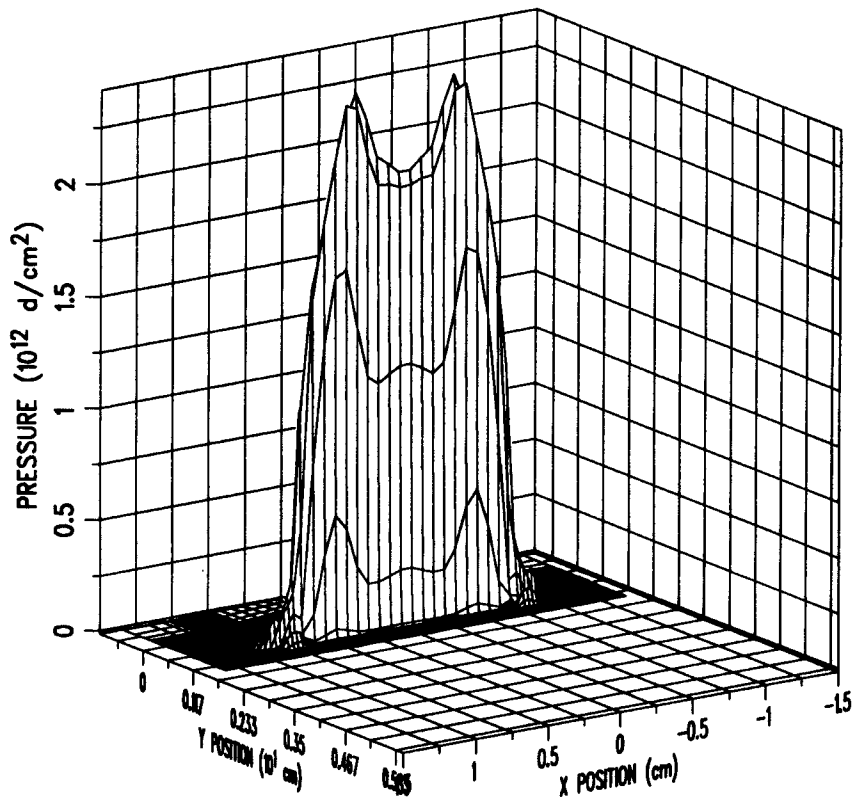


Fig. 10. Pressure profile 1.0 microseconds after end of x-ray deposition.

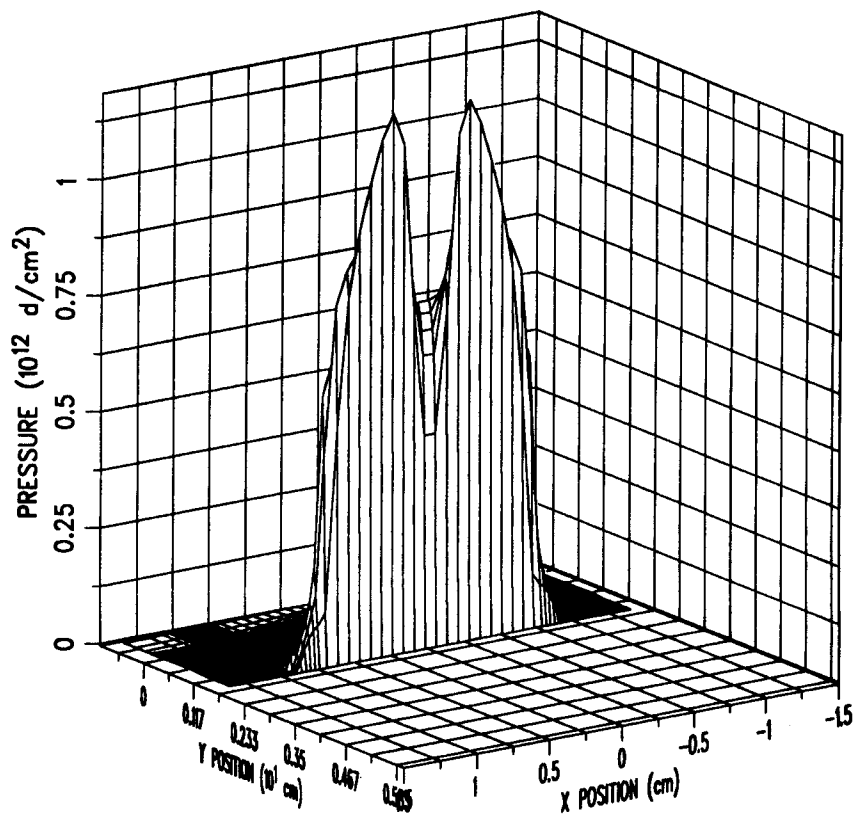


Fig. 11. Pressure profile 2.0 microseconds after end of x-ray deposition.

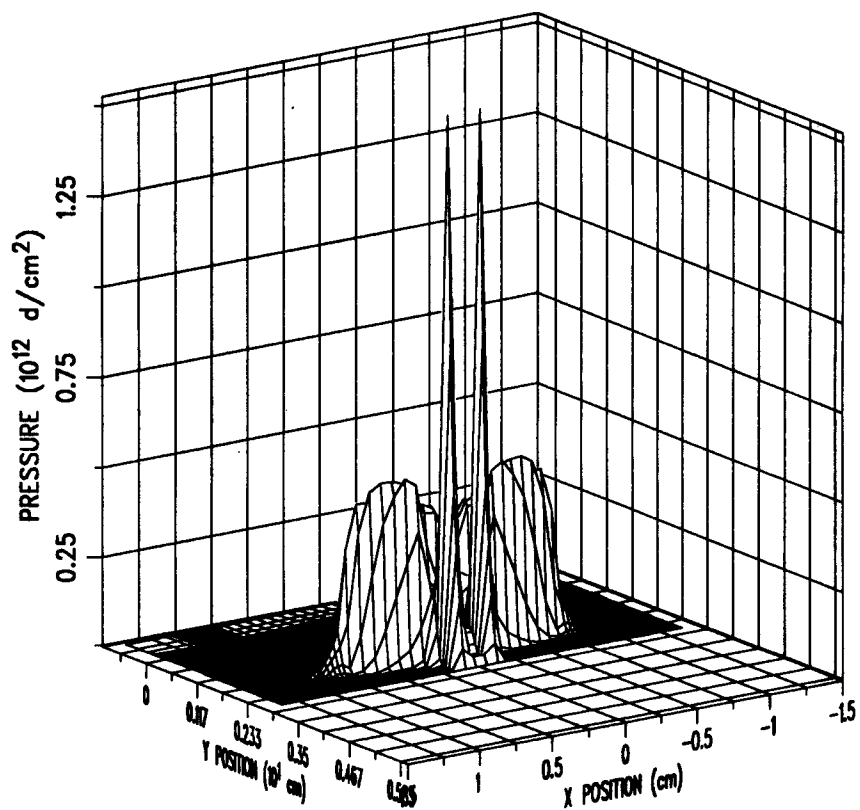


Fig. 12. Pressure profile 3.0 microseconds after end of x-ray deposition.

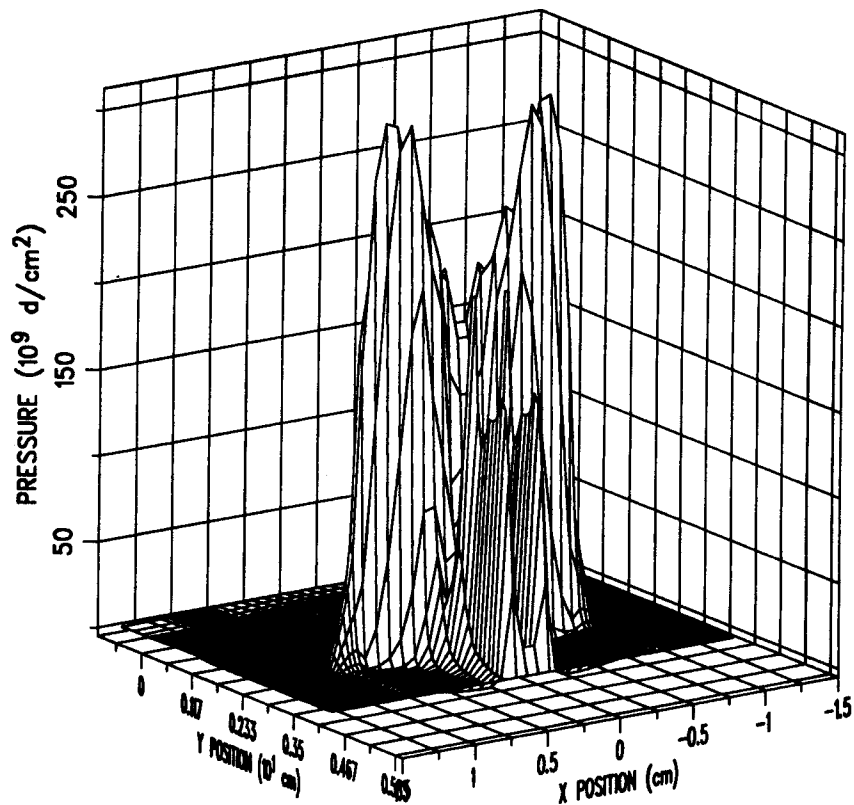


Fig. 13. Pressure profile 4.0 microseconds after end of x-ray deposition.

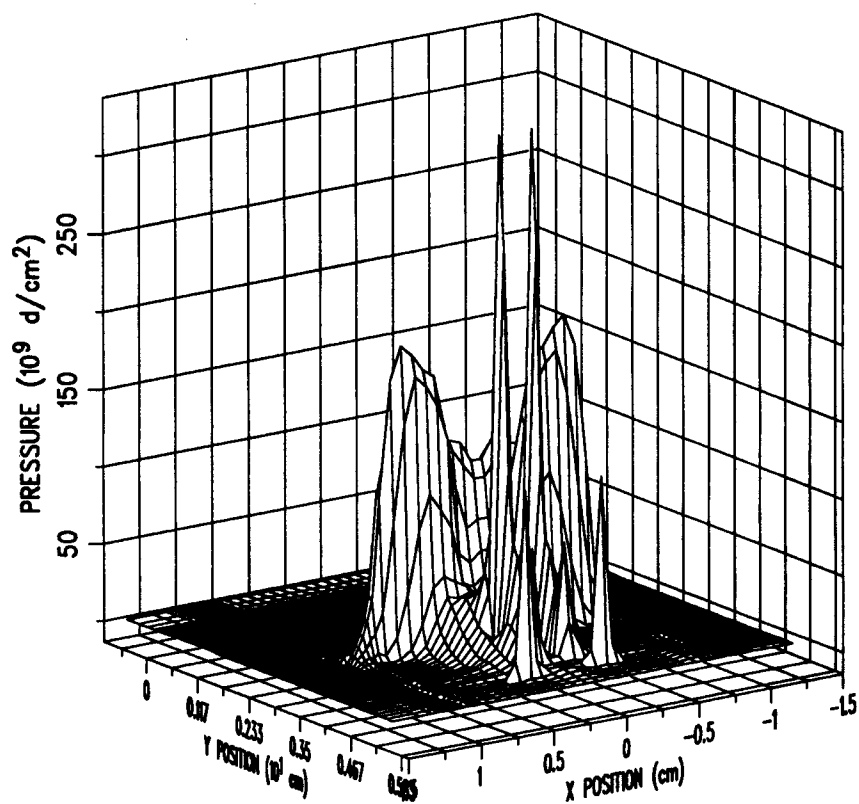


Fig. 14. Pressure profile 5.0 microseconds after end of x-ray deposition.

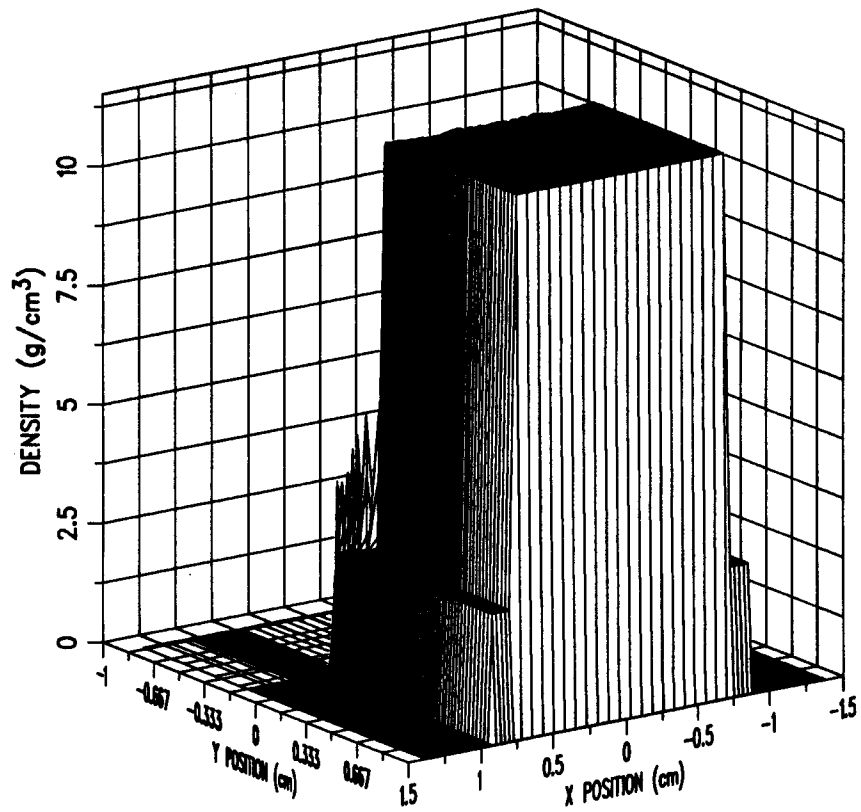


Fig. 15. Density profile 1.0 nanoseconds after end of x-ray deposition.

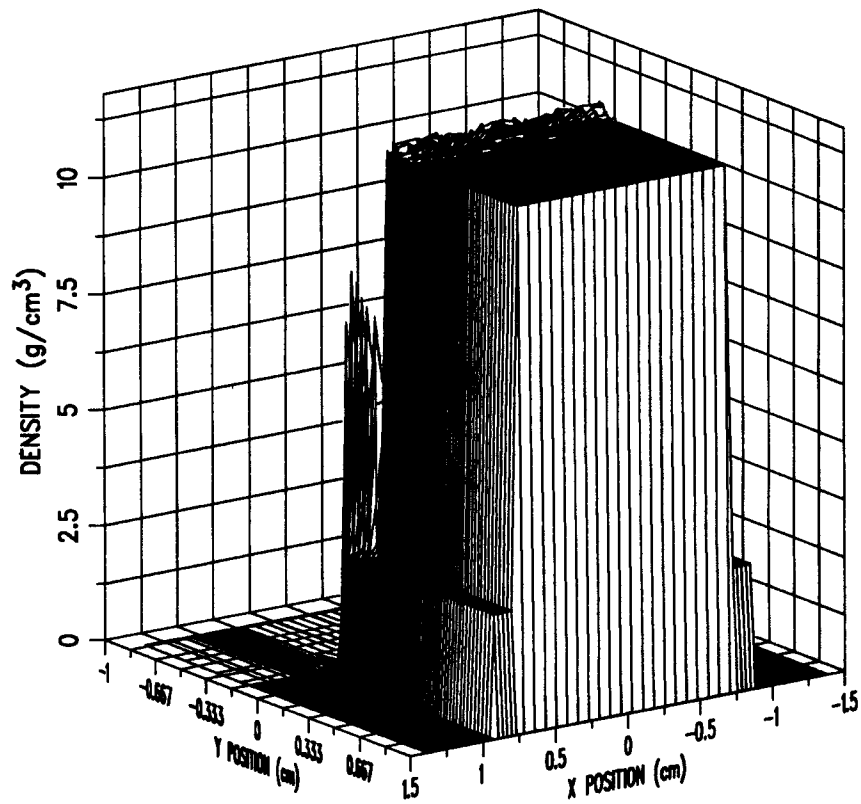


Fig. 16. Density profile 10.0 nanoseconds after end of x-ray deposition.

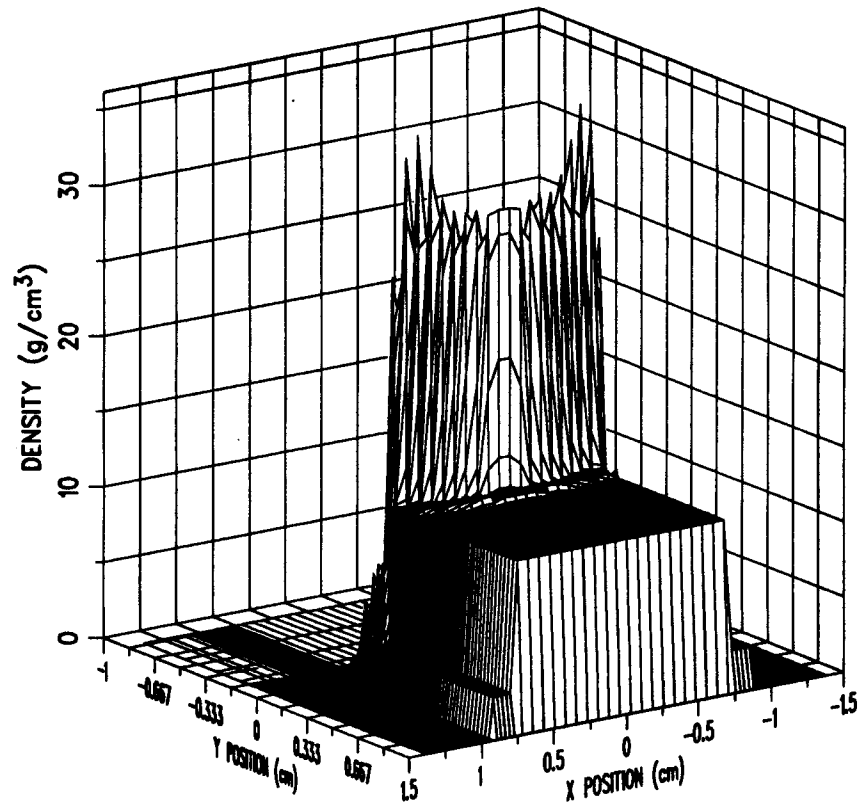


Fig. 17. Density profile 50.0 nanoseconds after end of x-ray deposition.

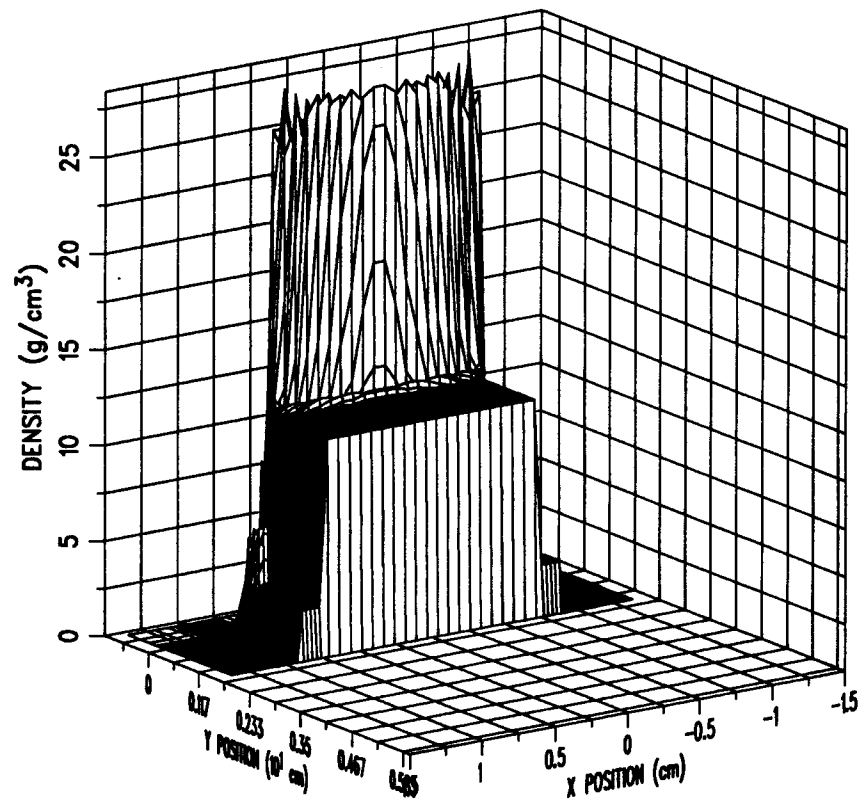


Fig. 18. Density profile 100.0 nanoseconds after end of x-ray deposition.

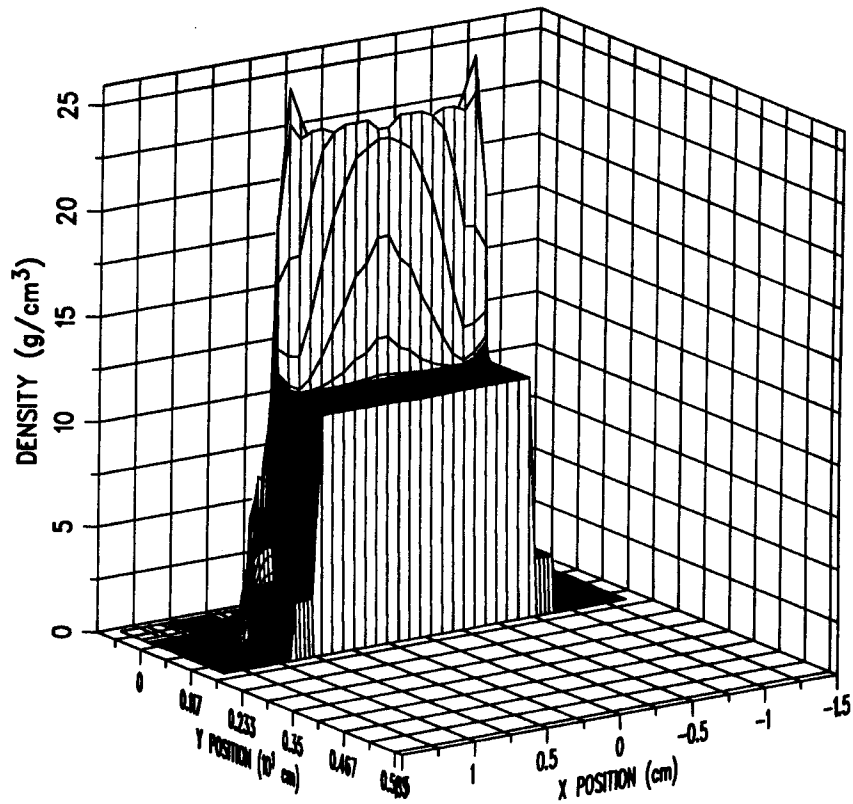


Fig. 19. Density profile 250.0 nanoseconds after end of x-ray deposition.

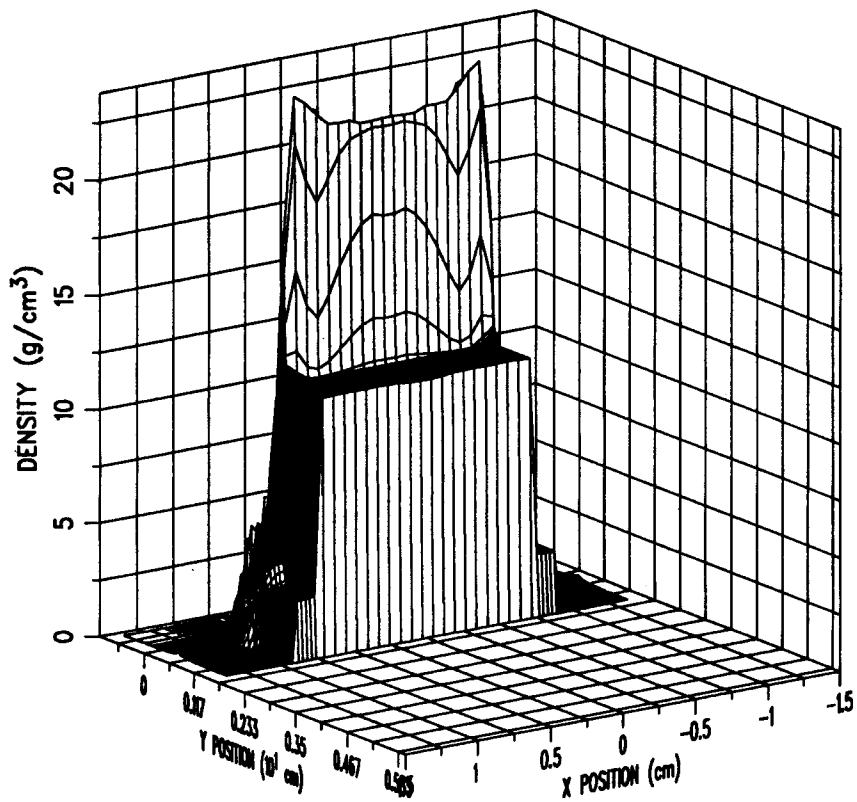


Fig. 20. Density profile 450.0 nanoseconds after end of x-ray deposition.

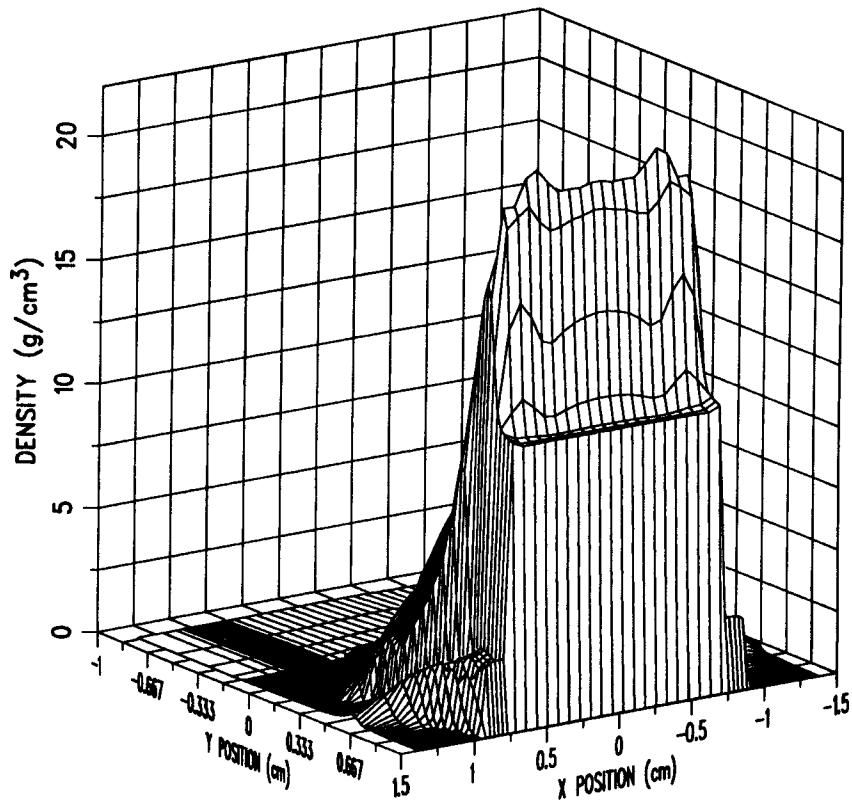


Fig. 21. Density profile 750.0 nanoseconds after end of x-ray deposition.

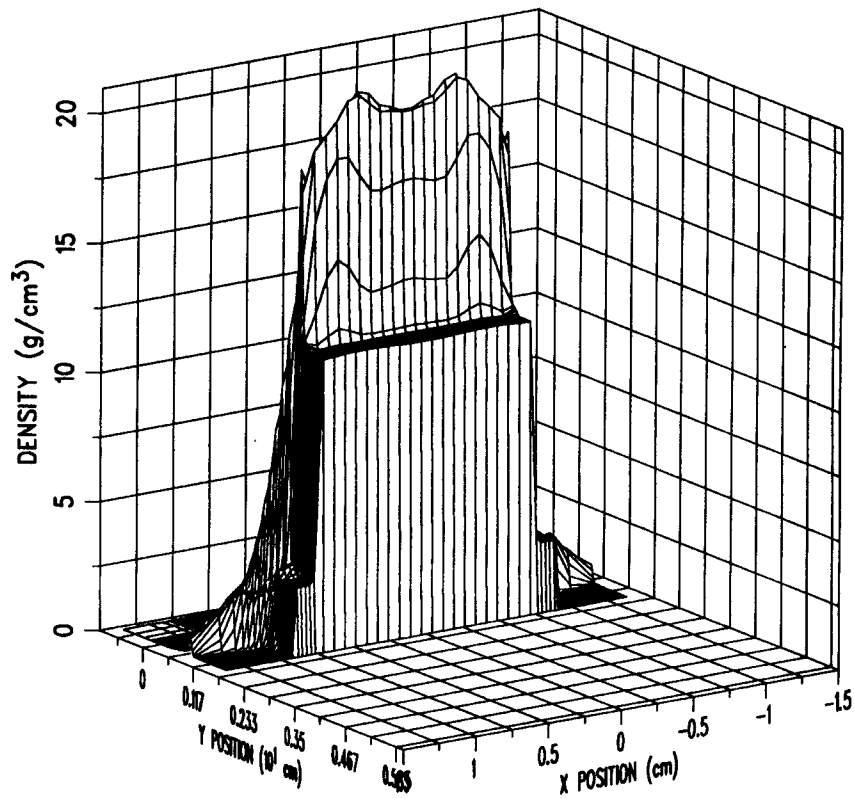


Fig. 22. Density profile 1.0 microseconds after end of x-ray deposition.

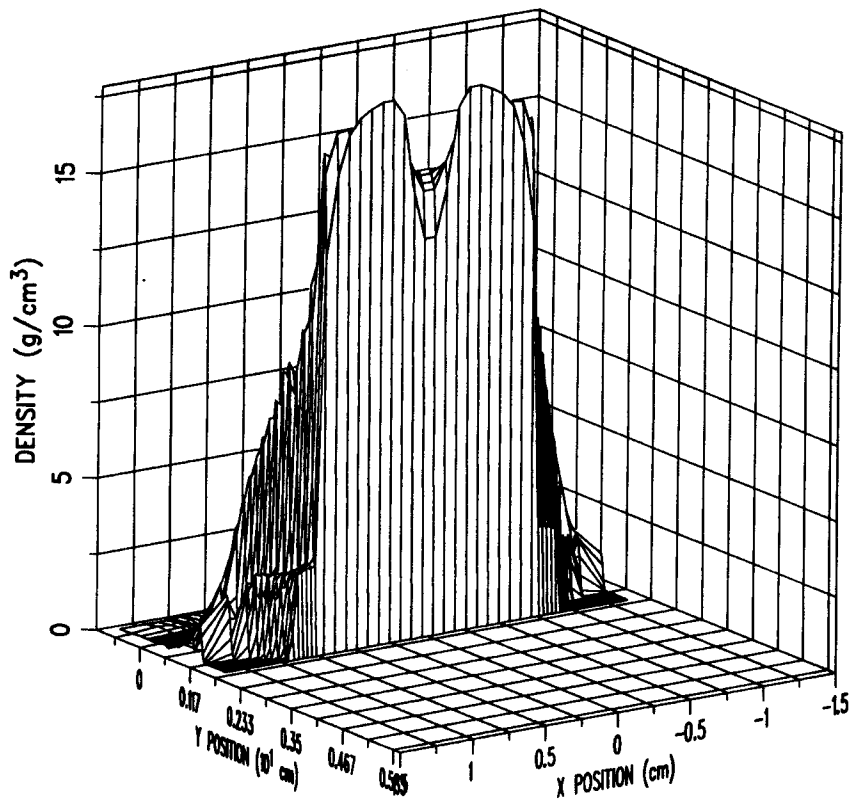


Fig. 23. Density profile 2.0 microseconds after end of x-ray deposition.

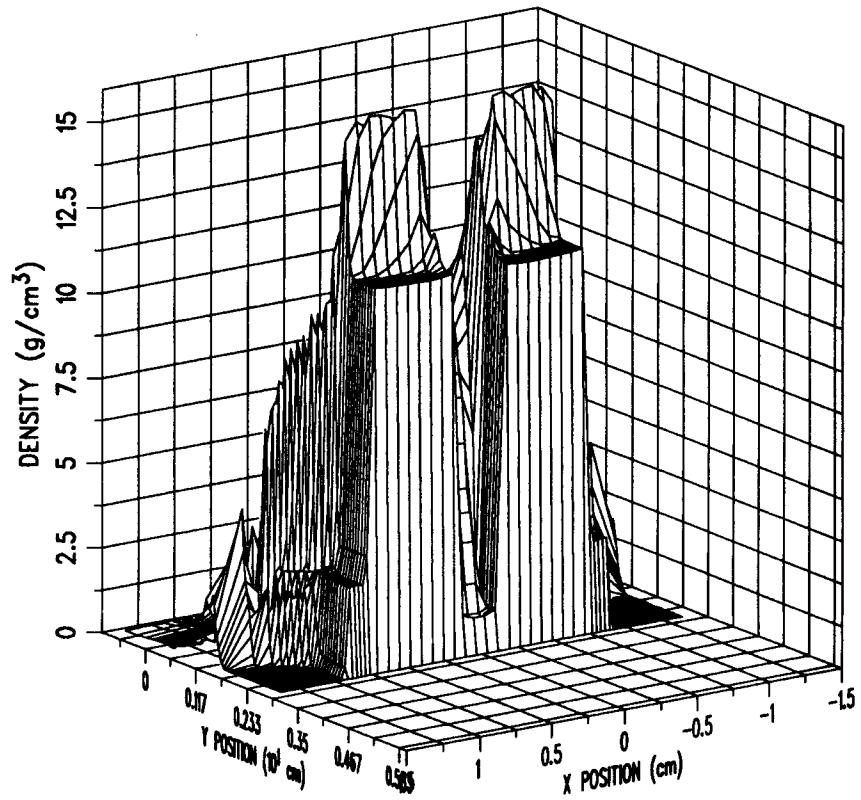


Fig. 24. Density profile 3.0 microseconds after end of x-ray deposition.

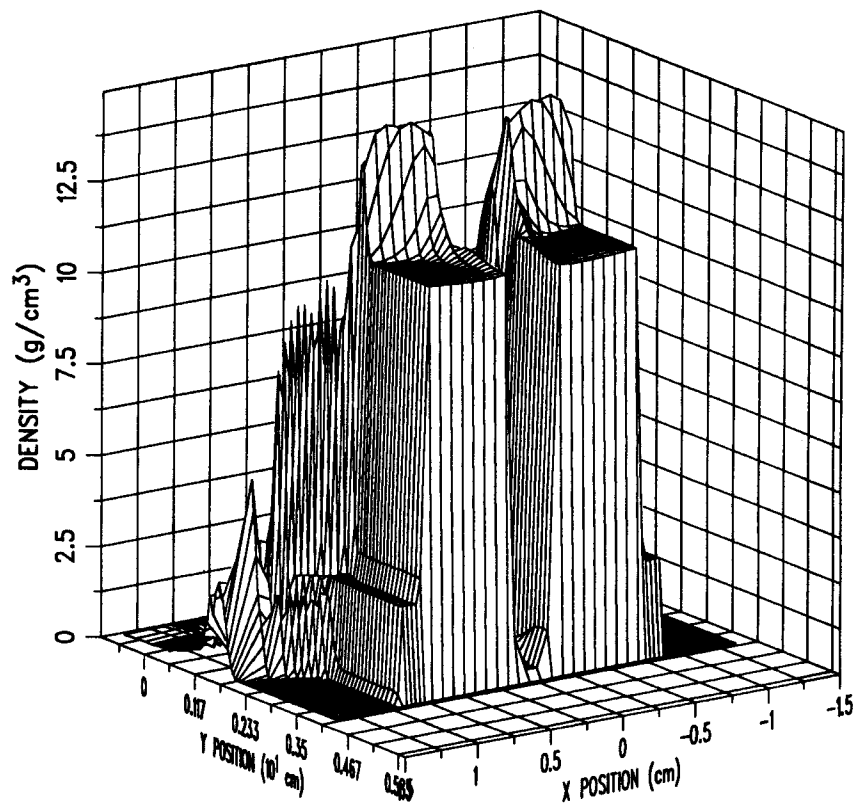


Fig. 25. Density profile 4.0 microseconds after end of x-ray deposition.

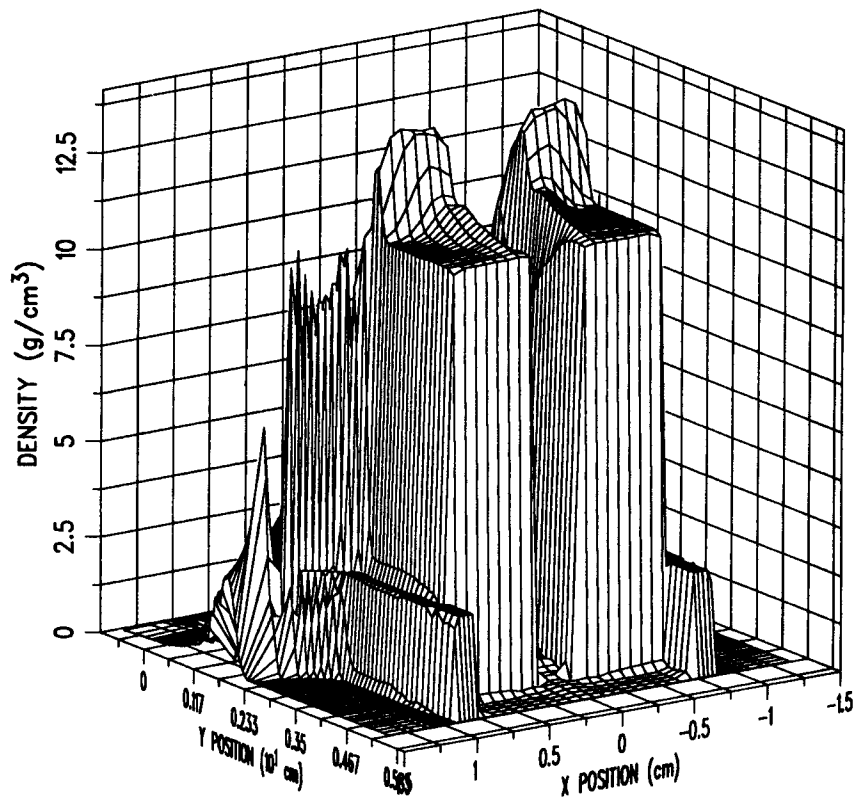


Fig. 26. Density profile 5.0 microseconds after end of x-ray deposition.

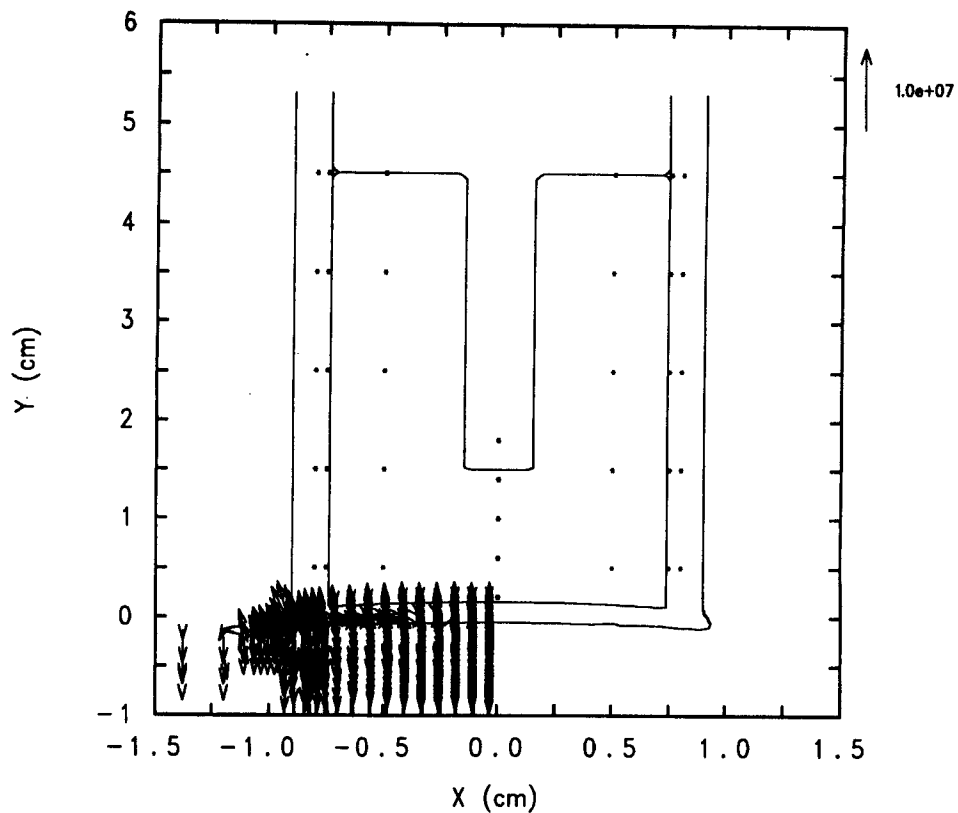


Fig. 27. Material interfaces and velocities 1.0 nanoseconds after end of x-ray deposition.

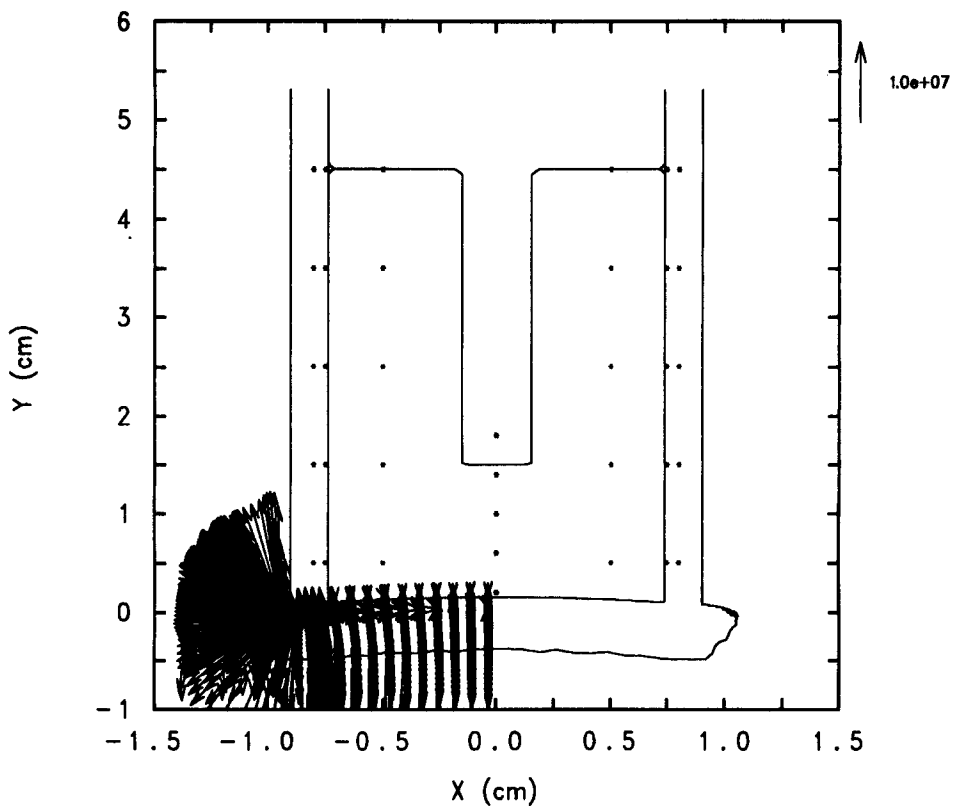


Fig. 28. Material interfaces and velocities 10.0 nanoseconds after end of x-ray deposition.

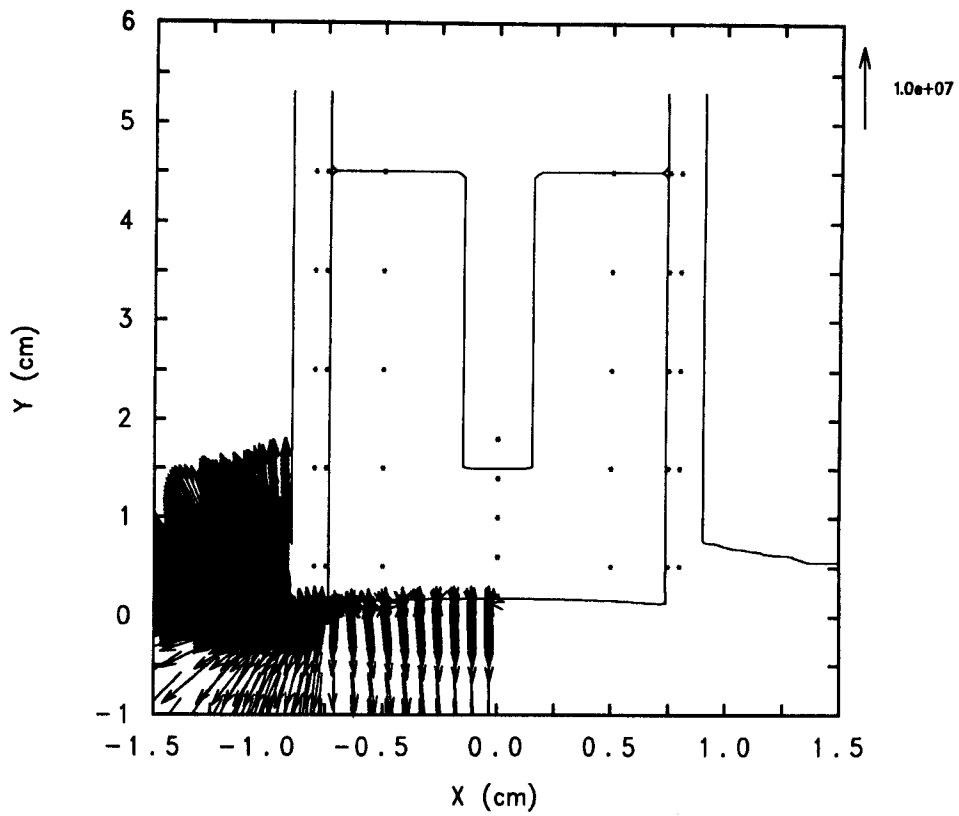


Fig. 29. Material interfaces and velocities 50.0 nanoseconds after end of x-ray deposition.

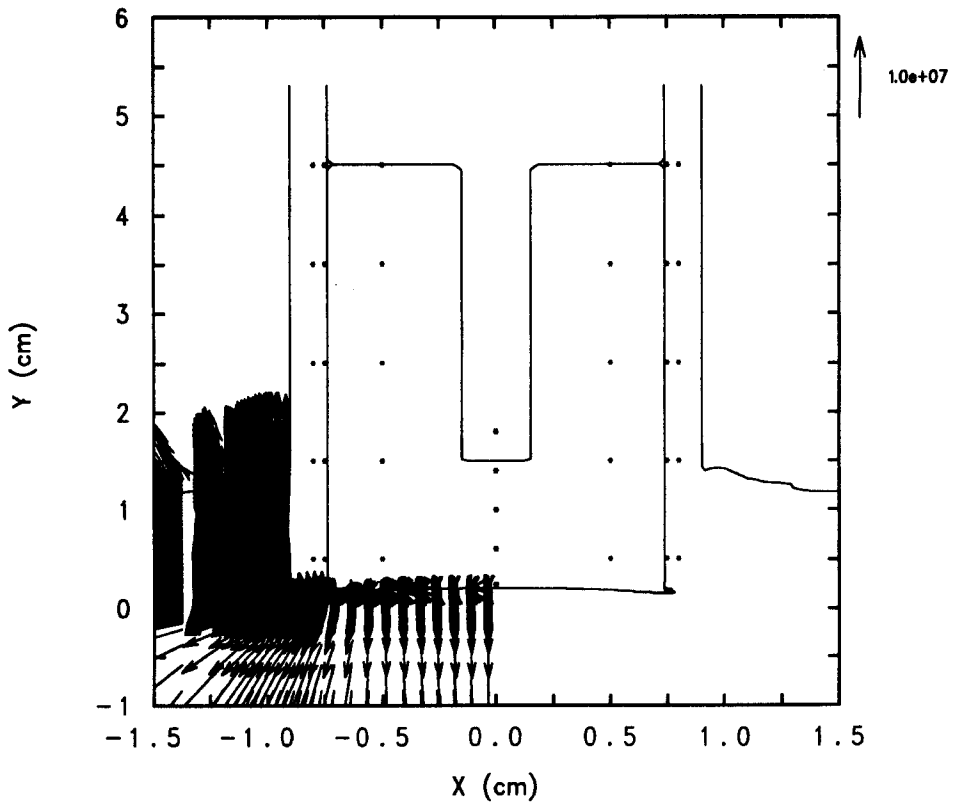


Fig. 30. Material interfaces and velocities 100.0 nanoseconds after end of x-ray deposition.

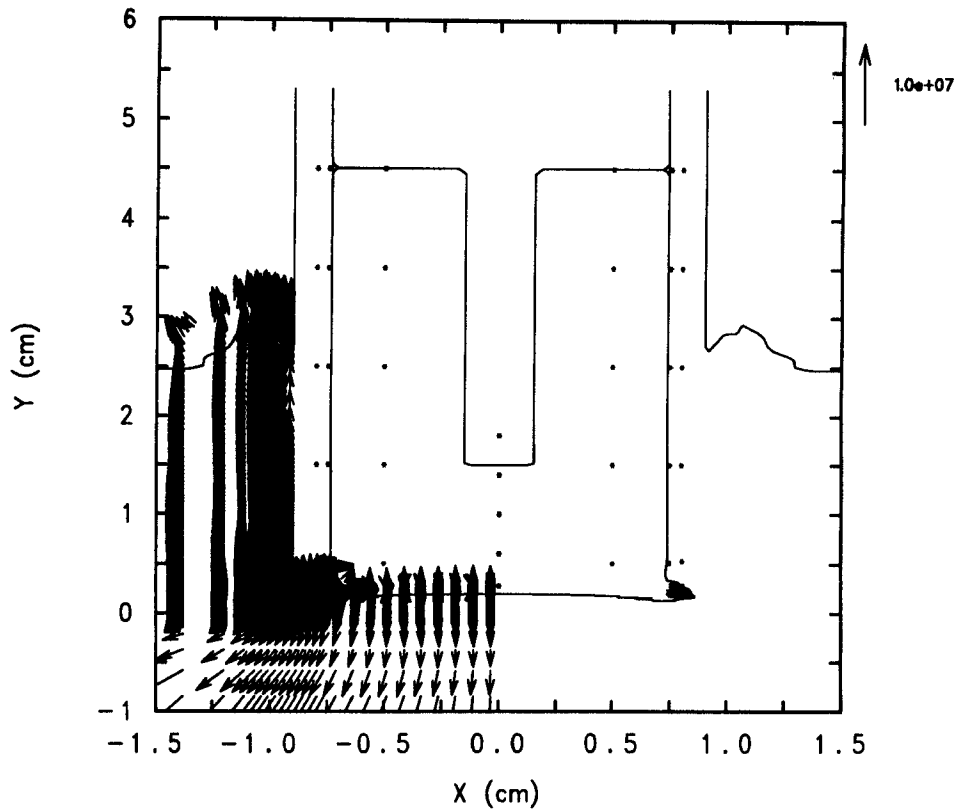


Fig. 31. Material interfaces and velocities 250.0 nanoseconds after end of x-ray deposition.

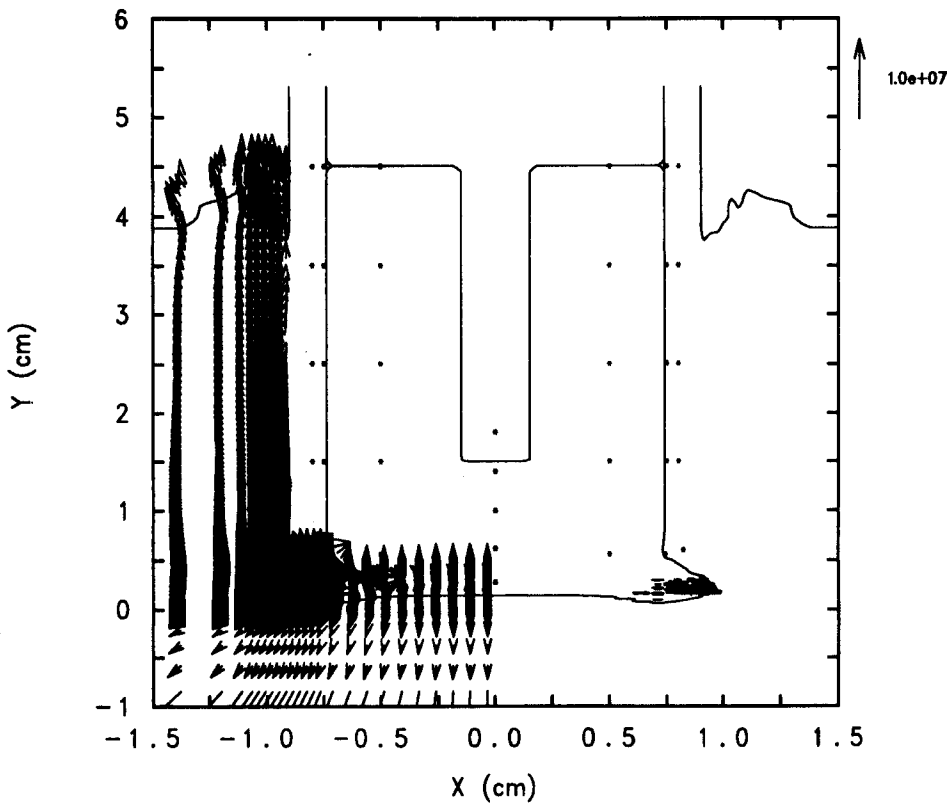


Fig. 32. Material interfaces and velocities 450.0 nanoseconds after end of x-ray deposition.

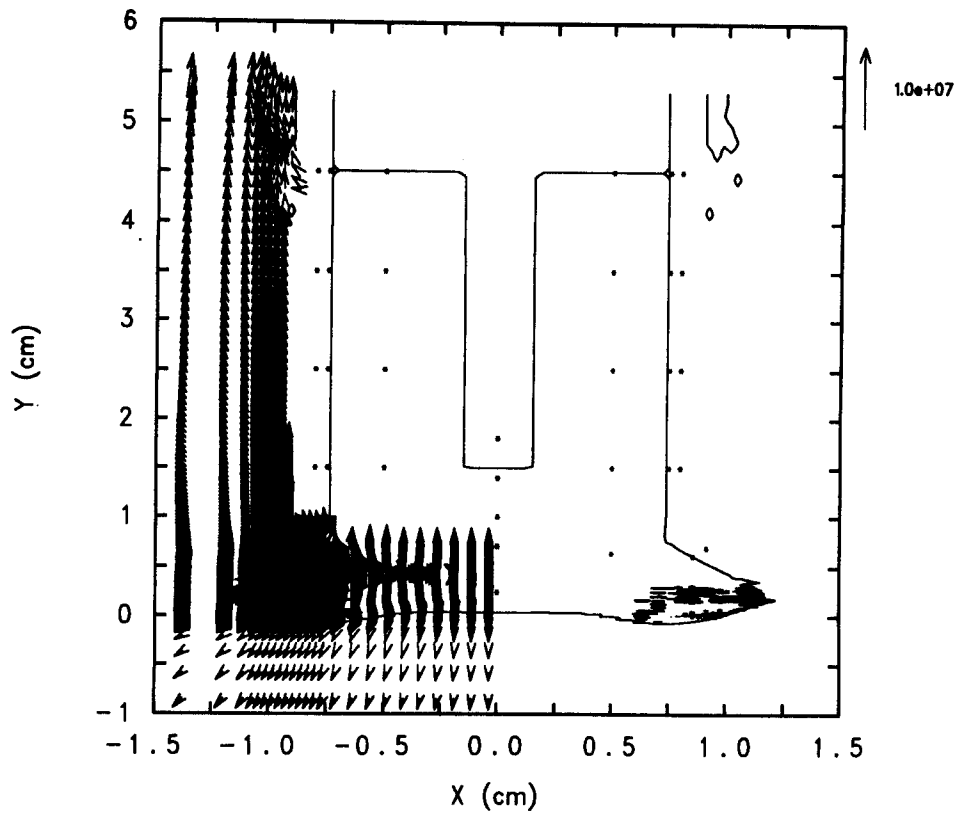


Fig. 33. Material interfaces and velocities 750.0 nanoseconds after end of x-ray deposition.

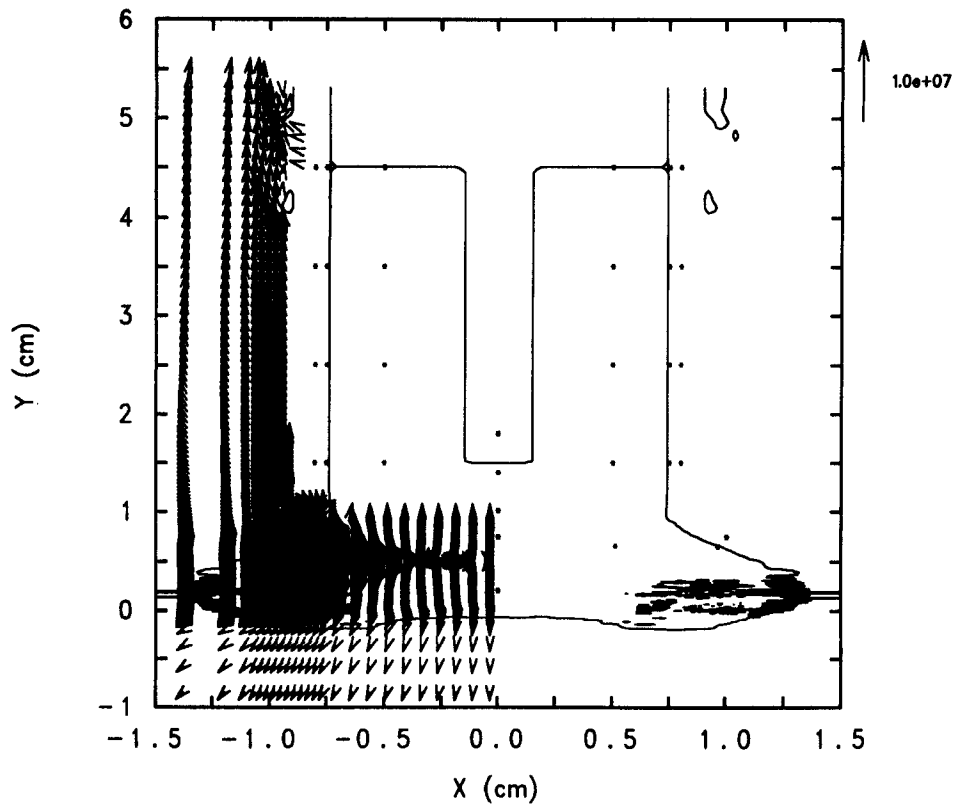


Fig. 34. Material interfaces and velocities 1.0 microseconds after end of x-ray deposition.

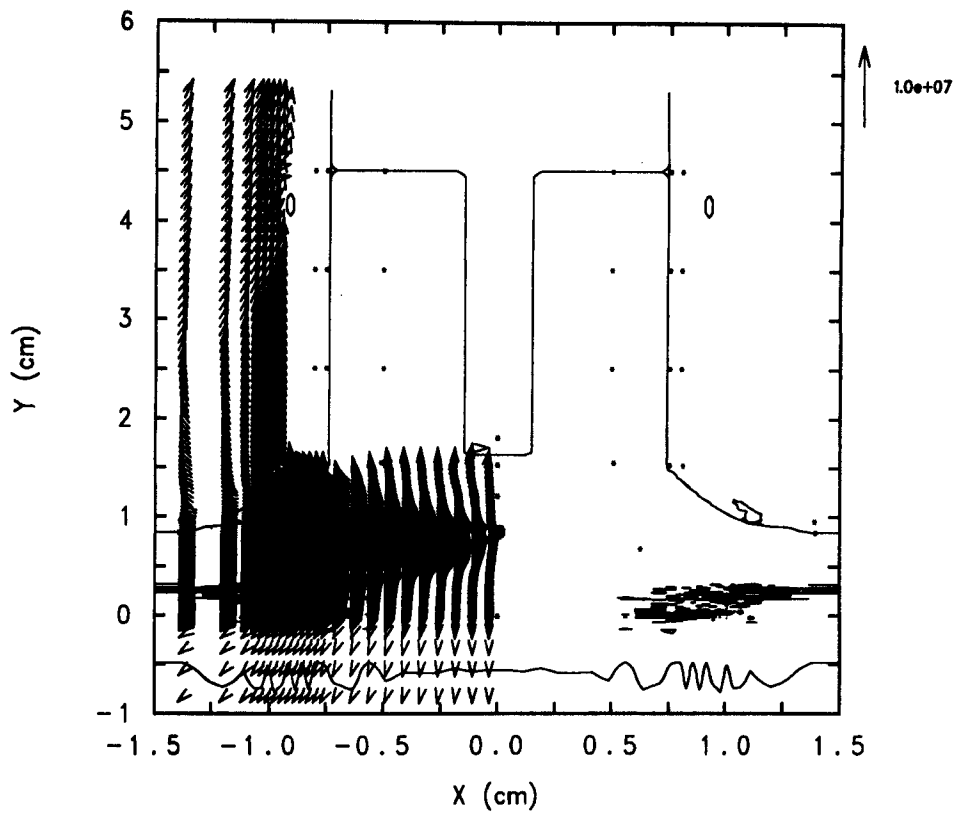


Fig. 35. Material interfaces and velocities 2.0 microseconds after end of x-ray deposition.

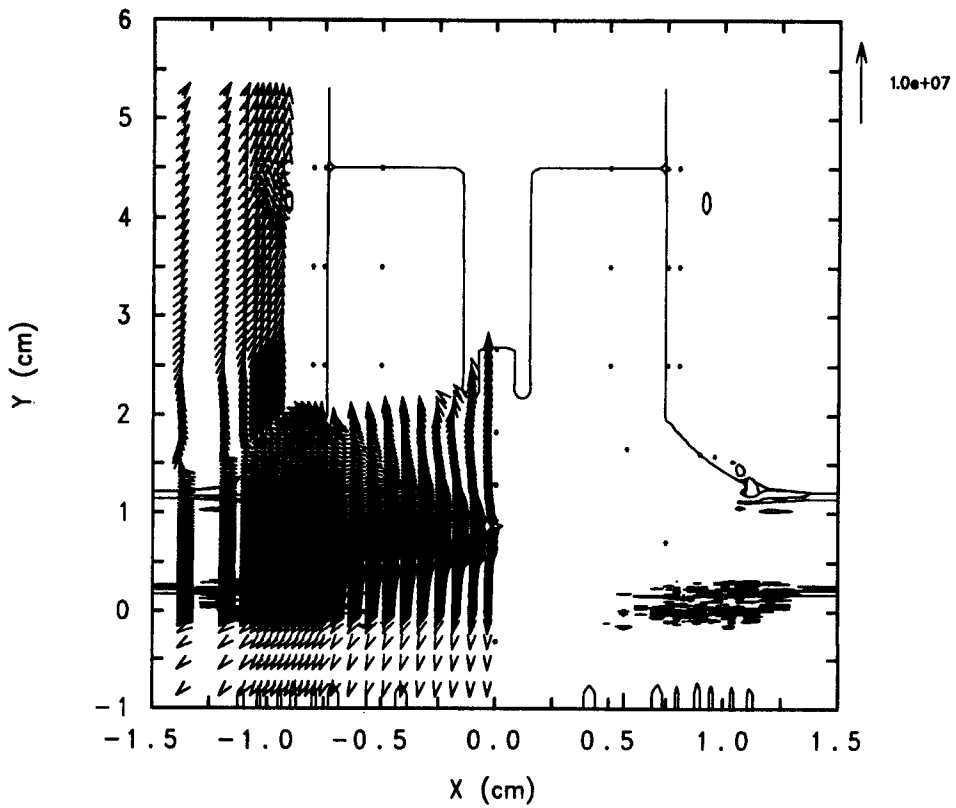


Fig. 36. Material interfaces and velocities 3.0 microseconds after end of x-ray deposition.

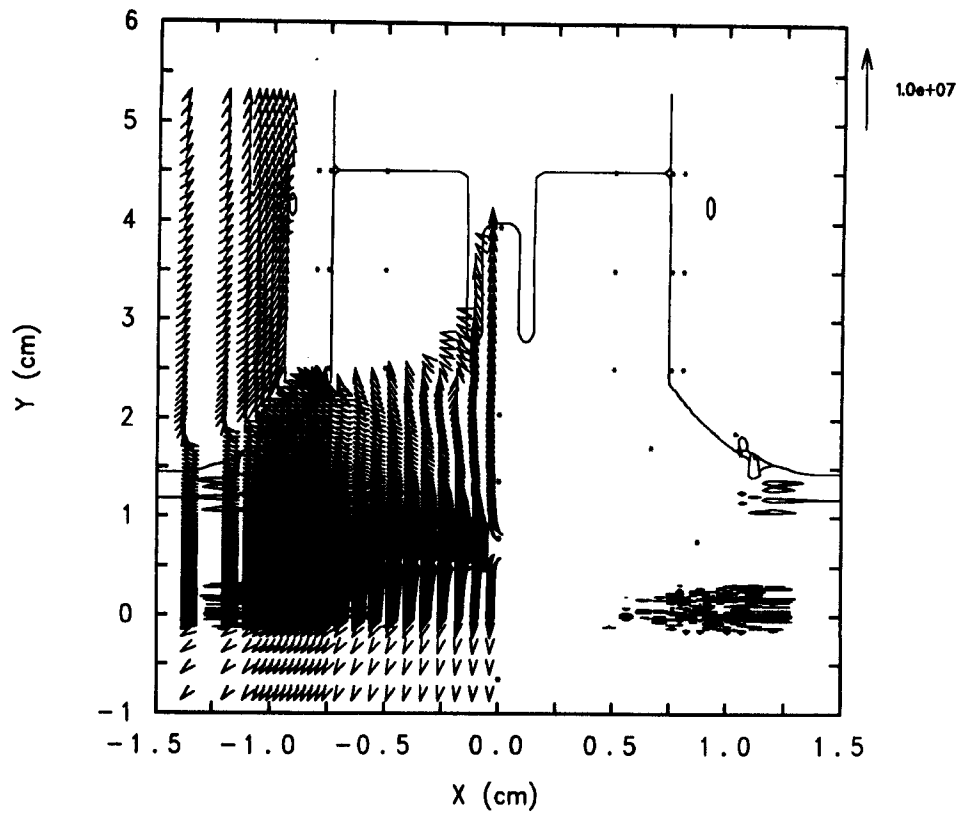


Fig. 37. Material interfaces and velocities 4.0 microseconds after end of x-ray deposition.

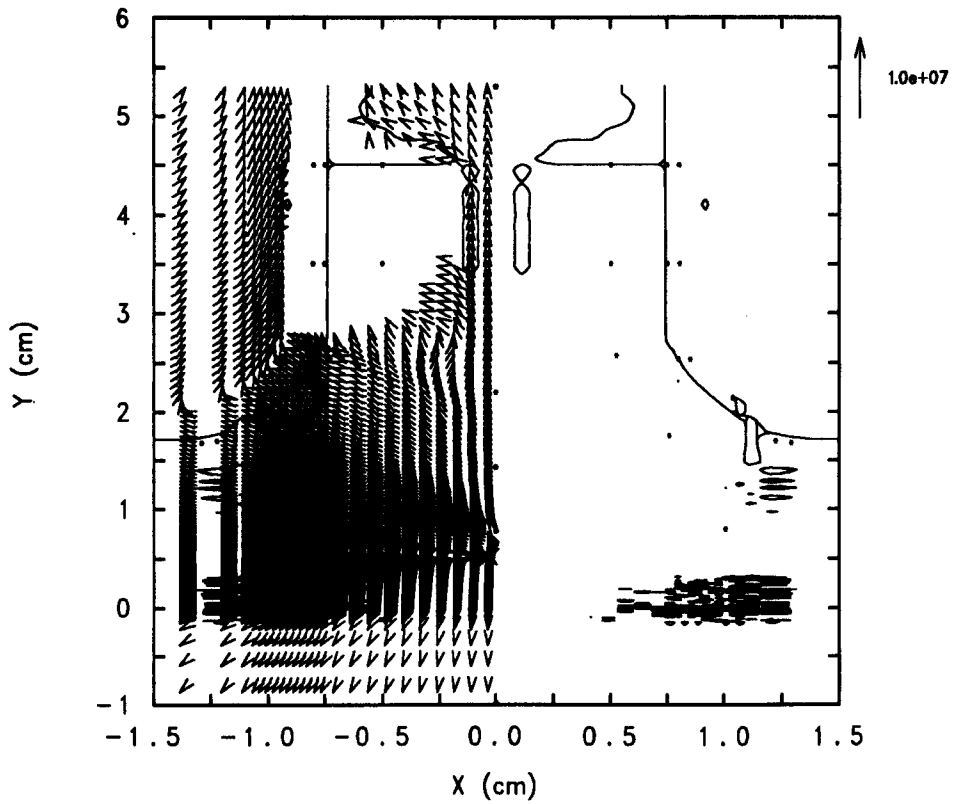


Fig. 38. Material interfaces and velocities 5.0 microseconds after end of x-ray deposition.

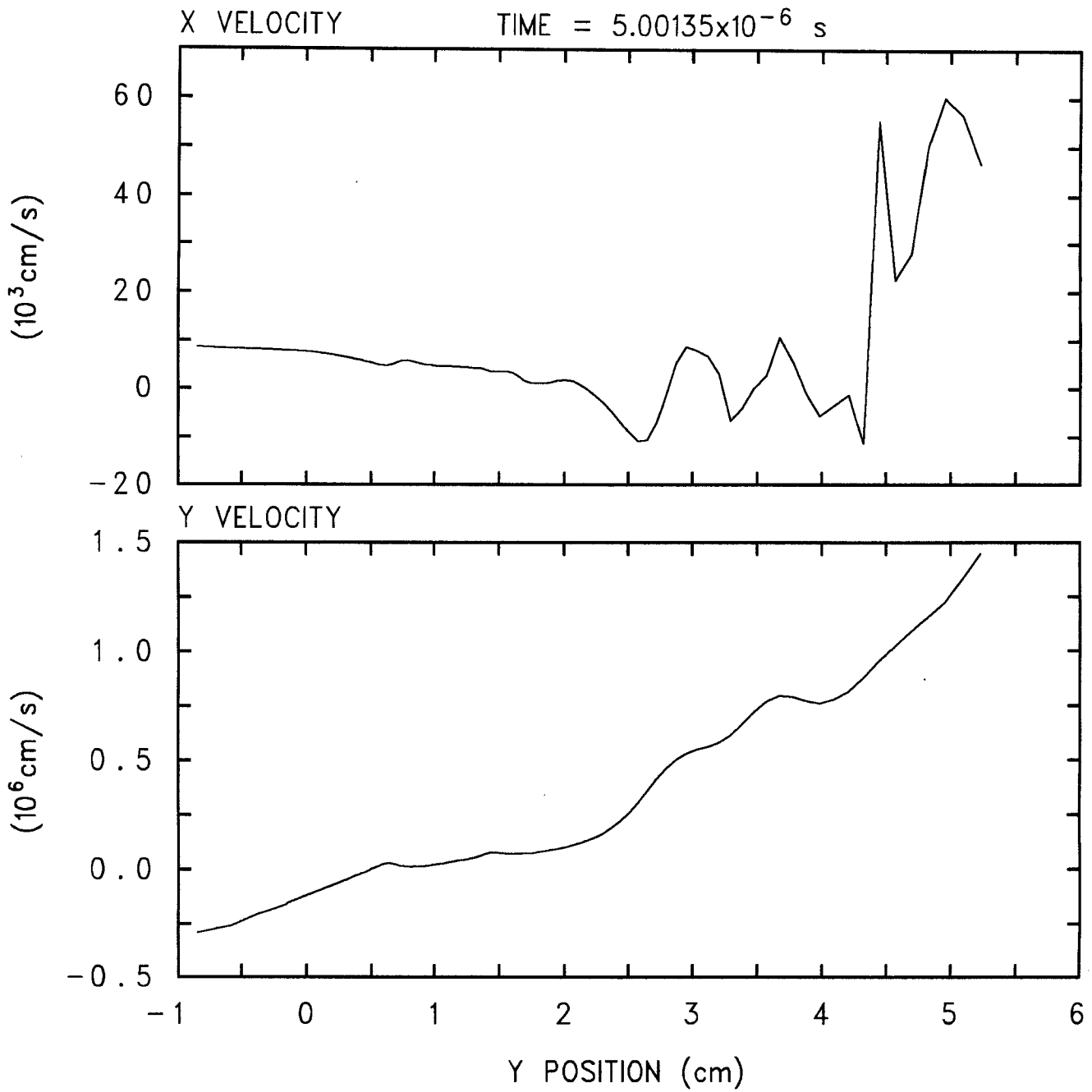


Fig. 39. Velocity profile on the centerline of the diagnostics package at 5.0 microseconds after the end of x-ray deposition.